revista principia

ISSN 2447-9187

https://doi.org/10.18265/2447-9187a2025id8833

ORIGINAL ARTICLE

SUBMITTED December 16, 2024

APPROVED May 30, 2025

PUBLISHED ONLINE July 2, 2025

FINAL FORMATTED VERSION March 6, 2026

ASSOCIATE EDITOR
Dr. Giovanilton Ferreira da Silva

Numerical study of cough droplets dispersion in indoor and quiescent environment: influence of droplet size and air humidity

Nuhu Ayuba [1] *

Gabriel Henrique Justi [2]

Gabriela Cantarelli Lopes [3]

[1] nuhu.ayuba101@gmail.com
[3] gclopes@ufscar.br
Federal University of São Carlos (UFSCar), São Carlos, São Paulo, Brazil

[2] gabrieljusti@unipampa.edu.br
Federal University of Pampa (UNIPAMPA), Bagé, Rio Grande do Sul, Brazil

* *Corresponding author.*

ABSTRACT: The transmission of infectious respiratory diseases (IRDs) has been widely studied across various fields using different methods. The emergence of SARS-CoV-2 (COVID-19) in late 2019 has increased the importance of such research. While many quantitative studies have examined how phase coupling, droplet size, and relative humidity affect respiratory droplet behavior, this study specifically looks at how these factors influence horizontal and vertical dispersion distances. It also evaluates the impact of phase coupling between the continuous and discrete phases. An Eulerian-Lagrangian approach was used to simulate droplet dispersion in a calm indoor environment under different humidity conditions. The results show that both droplet size and relative humidity significantly affect dispersion distances. Notably, smaller droplets (1 µm in diameter) evaporated almost instantly after release. Droplets measuring 10 µm traveled shorter horizontal and vertical distances under low humidity compared to higher humidity environments, where they evaporated quickly. Larger droplets (100 µm) formed more compact particle clouds and traveled shorter overall distances. Among the sizes tested, intermediate droplets (50 µm) created the most dispersed clouds, resulting in the greatest travel distances. At 80% relative humidity, these droplets reached a maximum horizontal distance of about 1.40 meters, the furthest noted in this study, highlighting a potential critical condition for airborne IRD transmission. Larger droplets tend to contribute more to surface contamination because they fall quickly, while the tiniest droplets pose less risk for airborne transmission due to their rapid evaporation. The effects of phase coupling on both horizontal and vertical dispersion were minimal. In conclusion, this study enhances understanding of environmental factors that influence IRD transmission in enclosed, still-air settings. Based on these findings, it is recommended that indoor environments maintain low relative humidity and adequate spacing between occupants to reduce the spread of droplets produced by coughing.

Keywords: computational fluid dynamics; Eulerian-Lagrangian model; phase coupling; respiratory droplet dispersion.

revista principia

ISSN 2447-9187

Estudo numérico da dispersão de gotículas de tosse em ambientes internos e quiescentes: influência do tamanho das gotículas e da umidade do ar

RESUMO: *A transmissão de doenças respiratórias infecciosas (DRIs) tem sido amplamente estudada em vários campos, usando diferentes métodos. O surgimento do SARS-CoV-2 (COVID-19) no final de 2019 aumentou a importância dessa pesquisa. Embora muitos estudos quantitativos tenham examinado como o acoplamento de fase, o tamanho da gota e a umidade relativa afetam o comportamento das gotas respiratórias, este estudo analisa especificamente como esses fatores influenciam as distâncias de dispersão horizontal e vertical. Ele também avalia o impacto do acoplamento de fase entre as fases contínua e discreta. Uma abordagem Euleriana-Lagrangiana foi usada para simular a dispersão de gotas em um ambiente interno calmo sob diferentes condições de umidade. Os resultados mostram que tanto o tamanho da gota quanto a umidade relativa afetam significativamente as distâncias de dispersão. Notavelmente, gotas menores (1 µm de diâmetro) evaporaram quase instantaneamente após serem liberadas. Gotas medindo 10 µm percorreram distâncias horizontais e verticais mais curtas sob baixa umidade em comparação com ambientes de alta umidade, onde evaporaram rapidamente. Gotas maiores (100 µm) formaram nuvens de partículas mais compactas e percorreram distâncias totais mais curtas. Entre os tamanhos testados, gotículas intermediárias (50 µm) criaram as nuvens mais dispersas, resultando nas maiores distâncias de viagem. A 80% de umidade relativa, essas gotículas atingiram uma distância horizontal máxima de cerca de 1,40 metro, a maior distância observada neste estudo, constituindo uma condição crítica potencial para a transmissão de DRIs pelo ar. Gotículas maiores tendem a contribuir mais para a contaminação de superfícies porque caem rapidamente, enquanto as gotículas menores representam menos risco de transmissão pelo ar devido à sua rápida evaporação. Os efeitos do acoplamento de fase na dispersão horizontal e vertical foram mínimos. Em conclusão, este estudo aumenta a compreensão dos fatores ambientais que influenciam a transmissão de DRIs em ambientes fechados e com ar parado. Com base nessas descobertas, recomenda-se que os ambientes internos mantenham baixa umidade relativa e espaçamento adequado entre os ocupantes para reduzir a propagação de gotículas produzidas pela tosse.*

Palavras-chave: *acoplamento de fase; dinâmica de fluidos computacional; dispersão de gotas respiratórias; modelo Euleriano-Lagrangiano.*

1 Introduction

Infectious Respiratory Diseases (IRDs), such as Severe Acute Respiratory Syndrome (SARS), tuberculosis (TB), and influenza (including avian and swine strains), have long been the focus of scientific research (Gupta; Lin; Chen, 2009; Morawska, 2006). In the early 1990s, the World Health Organization (WHO), working with governmental

and non-governmental organizations, called on the scientific community to develop strategies for managing transmissible diseases, especially influenza and TB (WHO, 1992).

The rapid and widespread spread of the SARS-CoV-2 virus, commonly known as COVID-19, in early 2020 (Kucharski *et al*., 2020), greatly heightened the urgency of IRD research, particularly strategies to control SARS-CoV-2 transmission in different environmental conditions.

Since the start of the pandemic, an estimated 700 million COVID-19 cases have been reported worldwide from January 2020 to April 2025, with the highest numbers in the United States (103 million), China (99.4 million), and India (45 million) (WHO, 2025). The impacts include a large loss of life, serious health issues, and significant economic downturns, especially in the most affected regions (Mishra *et al*., 2020).

Currently, research on IRDs extends beyond medical fields into areas such as engineering. While pathogens themselves may not be directly studied in engineering, parameters that influence the transport of contaminated respiratory droplets are of significant interest. Notable examples include particle size and velocity. For instance, larger droplets tend to settle quickly due to gravity, whereas smaller droplets are capable of traveling greater horizontal distances. Environmental factors such as relative humidity, temperature, wind speed, and direction also play important roles in the transmission of IRDs.

Most particles expelled during respiratory activities mainly consist of water (Li *et al*., 2018; Nicas; Nazaroff; Hubbard, 2005; Redrow *et al*., 2011). However, they may also carry virions (Branche; Falsey, 2015; Cole; Cook, 1998; Honkinen *et al*., 2012; Scharfman *et al*., 2016; Vejerano; Marr, 2018; Wölfel *et al*., 2020), as well as proteins, lipids, carbohydrates, DNA, and salts (Redrow *et al*., 2011).

The prevailing hypothesis suggests that airborne transmission occurs through clouds of droplets expelled during forceful respiratory events, such as coughing. Infection can happen either through direct inhalation (Han; Weng; Huang, 2013) or via indirect contact with contaminated surfaces (Aytogan; Ayintap; Yilmaz, 2020; Kampf *et al*., 2020), especially since large droplets, about 1,000 µm in diameter, settle quickly on nearby surfaces (Ningthoujam, 2020).

Different droplet size ranges have been reported in the literature. For example, Li *et al*. (2018) considered droplet sizes between 10 µm and 100 µm in their study of cough emissions. Gralton *et al*. (2011) and Perella *et al*. (2021) analyzed wider ranges, from 1 µm to 500 µm. Wei and Li (2015) indicated that cough-generated particles can vary from 1 µm to 1,000 µm. Weber and Stilianakis (2008) examined an even broader range, from 1 µm to 2,000 µm, covering most droplet sizes typically analyzed in Computational Fluid Dynamics (CFD) studies of IRD transmission.

In experimental studies, Lee *et al*. (2019) found that most droplets expelled by coughing were smaller than 5 µm. Similarly, Yang *et al*. (2007) reported an average droplet size distribution between 0.62 µm and 15.9 µm.

A comprehensive understanding of the fluid dynamics involved in respiratory events is thus critical to understanding and mitigating the spread of IRDs, particularly given the complexity of multiphase flows (Wang; Zeng; Yan, 2024; Zhao *et al*., 2010). For example, detailed information regarding temperature and humidity effects (Höppe, 1981), droplet sizes (Dbouk; Drikakis, 2020; Han; Weng; Huang, 2013; Redrow *et al*., 2011), droplet composition (Redrow *et al*., 2011), airflow direction (Gupta; Lin; Chen, 2009), evaporation processes (Chao *et al*., 2009; Han; Weng; Huang, 2013), and droplet fragmentation and distribution (Scharfman *et al*., 2016) can inform the design of more

effective protective masks, disinfection chambers, and social distancing policies, among other preventive strategies.

In CFD studies focused on IRDs, selecting the modelling approach is crucial. According to Feng *et al*. (2023), the Eulerian-Lagrangian and Eulerian-Eulerian frameworks are the most common methods for investigating the multiphase dynamics of respiratory droplets. The complexity of the flow, the definition of the computational domain, boundary conditions, mesh configuration, and the choice of physical and numerical models all play essential roles. For instance, within the Discrete Phase Modelling (DPM) or Euler-Lagrangian framework, physical models can incorporate parameters such as temperature-dependent latent heat, phase coupling, stochastic collisions, coalescence, and droplet breakup.

Phase coupling between continuous and discrete phases may be modelled as either one-way or two-way, depending on the objectives and scope of the CFD study. One-way coupling has been utilized by authors such as Li *et al*. (2020), Magar *et al*. (2021), Bahramian, Mohammadi and Ahmadi (2023), and Takii *et al*. (2022) whilst two-way coupling has been employed by researchers such as Dbouk and Drikakis (2020), Ge *et al*. (2022), Bahramian, Mohammadi and Ahmadi (2023) and Chillón *et al*. (2024).

While droplet behavior can be influenced by the continuous phase (i.e., the surrounding air), the reverse is also true. Phase coupling enables the exchange of heat, mass, and momentum between the discrete and continuous phases (ANSYS, 2012) and is crucial for precise flow simulations. Consequently, this study investigates the impact of phase coupling on the evaporation behavior of respiratory droplets in a quiescent indoor environment.

This type of environment was chosen because it simulates a typical room without natural airflow from doors and windows or artificial sources such as fans and air conditioning systems. While this setup limits generalizability to spaces with active airflow, it allows for controlled analysis of specific variables.

The aim is to compare simulation results using different coupling models. Additionally, the study explores how ambient relative humidity and droplet size influence the vertical and horizontal trajectories of respiratory droplets.

The results offer valuable insights into selecting coupling models that optimize computational efficiency and simulation accuracy. Furthermore, the findings enhance understanding of environmental conditions that may promote the spread and persistence of IRDs in enclosed, still-air spaces.

Such insights can guide the design of public indoor environments by recommending maintenance of low, yet health-safe, levels of relative humidity to reduce the persistence of potentially infectious droplets expelled through coughing.

The rest of this article is divided into the development of the mathematical models (Section 2). In Section 3, the numerical simulation setup is described. This is followed by a presentation and discussion of the results (Section 4), and finally, Section 5 concludes with a summary of the key findings.

2 Mathematical model

The CFD analysis of respiratory droplets can be conducted using two main modelling strategies: the Eulerian-Eulerian and Eulerian-Lagrangian approaches (Zahari *et al*., 2018). Since droplets expelled during coughing typically exhibit low mass loading, generally

below 10% to 12%, the Eulerian-Lagrangian model is regarded as more appropriate. In this approach, the continuous phase (air) is modelled using an Eulerian framework based on the Navier-Stokes equations, while the discrete droplet phase is tracked individually through a Lagrangian formulation.

This hybrid modelling technique enables a detailed analysis of droplet behaviour, including trajectory prediction, evaporation dynamics, and surface deposition, all of which are essential for understanding the transmission of airborne diseases (Gupta; Lin; Chen, 2009). Under low mass loading conditions, one-way coupling is often sufficient, as the dispersed phase exerts minimal feedback on the continuous phase (Bazant; Bush, 2021).

From a computational perspective, the Eulerian-Lagrangian method offers notable advantages, particularly in respiratory flow simulations. It reduces computational costs by focusing resources on tracking relevant droplets rather than resolving full droplet-fluid interactions across the entire domain, as required in Eulerian-Eulerian models (Dbouk; Drikakis, 2020). Additionally, this method supports the simulation of a wide range of droplet sizes under transient conditions, providing high numerical stability and flexibility. These qualities make it especially suitable for studies investigating coughing and sneezing events in indoor environments.

2.1 Eulerian model

In the present simulation, the continuous phase consists of air and water vapor. The key flow property of interest, density (ρ), is calculated according to Equation 1:

$$\rho_g = \sum Y_i \rho_i \tag{1}$$

where ρ_g represents the density of the air-water vapor mixture (in kg/m^3), and Y_i denotes the mass fraction of species i, with the constraint $\sum Y_i = 1$.

Determining the mass fraction of each component in the air-water vapor mixture is essential for accurate density estimation in multiphase flow simulations. In practical applications, the mass fraction of water vapor is often inferred from experimentally measured properties such as relative humidity (RH), temperature, and pressure. These parameters are typically obtained using instruments such as hygrometers, psychrometers, or humidity sensors (Sonntag *et al*., 2021; Wexler; Brombacher, 1951).

For the continuous phase, a single mass conservation equation governs the behavior of both air and water vapor, as shown in Equation 2.

$$\frac{\partial(\rho_g)}{\partial t} + \nabla \cdot (\rho_g \vec{u}_g) = \dot{m}_{d \to g} \tag{2}$$

where t is time (in s), $\vec{u}_g$ is the velocity vector of the continuous phase (in m/s), and $\dot{m}_{d \to g}$ is the mass source term representing the transfer of mass from the discrete phase (droplets) to the continuous phase (air-vapor mixture) due to evaporation. This term arises from the phase coupling between the Lagrangian and Eulerian phases.

Momentum conservation is the mixture is expressed through a single equation, since all phases are subjected to same influences, namely, pressure, gravity, viscous stress, and momentum exchange with the discrete phase, as given by Equation 3:

$$\frac{\partial(\rho_g \vec{u}_g)}{\partial t} + \nabla \cdot (\rho_g \vec{u}_g \vec{u}_g) = -\nabla P_g + \nabla \cdot \tau_g + \vec{F}_g \tag{3}$$

where P_g is pressure (in Pa), τ_g is the viscous stress tensor (in Pa), $\vec{F}_g$ is the volumetric force vector.

Similar, the conservation of energy for the continuous phase is described by Equation 4:

$$\frac{\partial(\rho_g h_g)}{\partial t} + \nabla \cdot (\rho_g \vec{u}_g h_g) = \nabla \cdot (\tau_g \cdot \vec{u}_g) - \nabla \cdot \vec{q}_g - \dot{m}_{d \to g} h_{d,g} \tag{4}$$

where h_g (in J/kg) is the specific enthalpy of the continuous phase, q_g is the heat flux vector (in W/m^2), $\dot{m}_{d \to g}$ is the mass transfer rate from droplets to the continuous phase (in kg/m^3.s), and $h_{d,g}$ is the specific enthalpy of the evaporated mass (in J/kg). This equation encapsulates energy transport in a multiphase system, where energy exchange occurs at the phase interface due to evaporation. The left-hand side denotes the temporal and convective transport of enthalpy, while the right-hand side includes mechanical work from viscous forces, conductive heat transfer (typically modeled using Fourier's law), and energy exchange resulting from phase transitions.

2.1.1 Closure equations

In this study, droplets ranging in size from 1 µm to 100 µm were considered. According to Hinds and Zhu (2022) and Sirignano (2009), droplets smaller than 10 µm typically undergo diffusion-limited evaporation, with negligible convective enhancement due to their low Reynolds numbers (Re << 1). For intermediate-sized droplets, approximately 10 µm to 50 µm, both diffusion and convection significantly influence the mass transfer process. Droplets larger than 50 µm, particularly those approaching 100 µm, are generally classified as large droplets, for which convective effects dominate evaporation (ANSYS, 2012; Sirignano, 2009). For droplets around 100 µm, external convection substantially enhances vapor removal, especially under the high relative velocities associated with respiratory flows such as coughing.

The evaporation of smaller cough droplets is governed by the diffusive flux of droplet vapor into the surrounding air (Li *et al.*, 2020). In the simulations presented in this study, evaporation is assumed to begin when the droplet temperature, T_d, reaches the vaporization temperature, T_v. Evaporation continues until the droplet fully disappears or reaches the boiling temperature, T_b, as represented in Equation 5:

$$T_v \leq T_d < T_b \tag{5}$$

When the evaporation rate is slow, it is primarily governed by gradient diffusion. In this case, the vapor transition from the droplet surface to the gas phase is driven by the

concentration difference between the droplet surface and the bulk gas. The corresponding rate of mass change for the droplet is given by Equation 6:

$$\frac{Dm_d}{Dt} = -k_c\left(C_{v,d} - C_{d,\infty}\right)\ A_d MW_w \tag{6}$$

Here, k_c is the mass transfer coefficient (in m/s); $C_{v,d}$ and $C_{w,\infty}$ are the water vapor concentrations at the droplet surface and in the bulk gas, respectively (in kmol/m^3); A_d is the droplet surface area (in m^2); and MW_w is the molecular weight of water (in kg/kmol).

The mass transfer coefficient is calculated using the Froessling correlation (Equation 7), which relates the Sherwood number (*Sh*) to the Reynolds (*Re*) and Schmidt (*Sc*) numbers:

$$Sh = \frac{k_c d_d}{D_v} = 2 + \frac{3\,\mathrm{Re}_d^{1/2} Sc^{1/3}}{5} \tag{7}$$

In this equation, D_v is the diffusion coefficient of water vapor in air (in m^2/s), and d_d is the droplet diameter (in m). The correlation is valid for Reynolds numbers between 2 and 800, and Schmidt numbers ranging from 0.6 to 2.7. The dataset used from Evnochides and Thodos supports this correlation for *Re* values between 1,500 and 12,000 and *Sc* values between 0.6 and 1.85, which aligns with the conditions in this study.

At the droplet surface, where the temperature is T_d, the vapor concentration is calculated under the assumption that the partial pressure of vapor equals the saturation pressure (P_{sat}), as shown in Equation 8:

$$C_{v,d} = \frac{P_{sat}}{R\,T_d} \tag{8}$$

where R is the universal gas constant (atm.L.mol^{-1}.K^{-1}).

The concentration of water vapor in the bulk gas is estimated using Equation 9:

$$C_{v,\infty} = \frac{p}{R\,T_\infty} Y_v \tag{9}$$

where p is the absolute pressure (Pa), T_∞ is the ambient air temperature (K), and Y_v is the local mole fraction of the water vapor in the bulk gas.

For larger cough droplets, convective effects become relevant and must be incorporated into the evaporation model. Li *et al*. (2018) and Li *et al*. (2020) proposed the following formulation for the evaporation rate from the droplet surface to the bulk gas phase (Equation 10):

$$\frac{dm_d}{dt} = k_c A_p \rho_\infty \ln\left(1 + \frac{Y_{v,d} - Y_{v,\infty}}{1 - Y_{v,d}}\right) \tag{10}$$

where ρ_∞ is the density of the bulk gas (air), $Y_{v,d}$ and $Y_{v,\infty}$ are the vapor mass fraction at the droplet surface and in the bulk gas, respectively.

During the evaporation process, the droplet temperature is updated based on the heat balance between the droplet and the surrounding fluid, as expressed in Equation 11:

$$m_d c_d \frac{dT_d}{dt} + \frac{dm_d}{dt} h_{fg} = h A_d \left(T_\infty - T_d \right) \tag{11}$$

where c_d is the specific heat of the droplet ($J.kg^{-1}.K^{-1}$), h_{fg} is the latent heat of vaporization ($J.kg^{-1}$), and h is the convective heat transfer coefficient ($W.m^2.K^{-1}$)

All the equations used in this section are derived from the FLUENT Theory Guide (ANSYS, 2012).

2.1.2 Turbulence modeling

The turbulence model forms part of the closure equations. In this study, the Shear Stress Transport (SST) k-ω model was adopted due to its capability to simulate flows with adverse pressure gradients. This model is known for providing accurate turbulence prediction both near the walls and in the free stream (Ayuba; Lopes, 2023; Li *et al*., 2020; Menter; Kuntz; Langtry, 2003; Pokharel *et al*., 2021; Wai *et al*., 2020).

The SST k-ω model, developed by Menter, Kuntz and Langtry (2003), blends the standard k-ε and k-ω models using switching (blending) function that activates the k-ω formulation near walls and the k-ε formulation in the outer flow region. The specific dissipation rate ω is given by:

$$\omega = \frac{\varepsilon}{k} \tag{12}$$

The transport equations of the SST k-ω model are given as follows:

$$\frac{\partial}{\partial t}\left(\rho_g k\right) + \nabla \cdot \left(\rho_g k u_g\right) = \nabla \cdot \left(\Gamma_k \nabla k\right) + \widetilde{G}_k - Y_k \tag{13}$$

$$\frac{\partial}{\partial t}\left(\rho_g \omega\right) + \nabla \cdot \left(\rho_g \omega u_g\right) = \nabla \cdot \left(\Gamma_\omega \nabla \omega\right) + G_\omega - Y_\omega \tag{14}$$

where k denotes the turbulent kinetic energy, Γ_k and Γ_w are the effective diffusivities of k and i, respectively. Y_k and Y_w represent the dissipation rates of k and ω, respectively. $\widetilde{G}_k$ and G_w account for turbulence production due to mean velocity gradients.

2.2 Lagrangian model

In the Discrete Phase Model (DPM), the continuous fluid phase is solved using the Eulerian approach (as outlined in subsection 2.1), while the dispersed phase is modeled by tracking numerous individual particles through the precomputed flow field. The dispersed phase interacts with the fluid phase through the exchange of momentum, mass, and energy.

Within multiphase flow simulations, the DPM calculates individual particle trajectories at discrete time intervals, making it particularly suitable for studying the dynamics of human coughs. In the standard formulation of the Lagrangian multiphase model, it is assumed that the volume fraction of the dispersed phase remains sufficiently low. The mass formulation is presented in Equation 15:

$$\frac{d\,u_d}{dt} = F_D\left(\vec{u}_g - \vec{u}_d\right) + \vec{g}\,\frac{\rho_d - \rho_g}{\rho_d} \tag{15}$$

where $\vec{u}_g$ is the velocity of the continuous phase, $\vec{u}_d$ is the droplet velocity, and ρ_d is the droplet density. F_D is the drag force per unit particle mass, expressed in Equation 16 (ANSYS, 2012).

$$F_D = \frac{18\,\mu_g}{\rho_d\,d_d^2} \times \frac{C_D\,\mathrm{Re}}{24} \tag{16}$$

Here, Re is the particle Reynolds number, and C_D is the drag coefficient for spherical particles, given by the Schiller and Naumann model (1935), as shown in Equations 17 and 18:

$$\Re = \frac{\rho_g\,d_d\left|\vec{u}_d - \vec{u}_g\right|}{\mu_g} \tag{17}$$

$$C_D = \begin{cases} \dfrac{24\left(1 + 0.15\,\Re^{0.687}\right)}{\mathrm{Re}} & for\ \ \Re \le 1000 \\ 0.44 & for\ \ \Re > 1000 \end{cases} \tag{18}$$

Equation 18 demonstrates that the drag coefficient depends on the particle Reynolds number and is defined piecewise according to its magnitude.

2.2.1 Stochastic tracking

Particle dispersion caused by turbulence in the fluid phase can be modeled using either the stochastic tracking model or the particle cloud model. Among the stochastic approaches, the Discrete Random Walk (DRW) and Continuous Random Walk (CRW) models are widely used in CFD studies of cough-droplet dispersion due to their computational efficiency and ability to capture general trends of turbulence-induced dispersion.

In the present work, the stochastic tracking approach, commonly known as the random walk model, was employed. This method simulates the effect of instantaneous turbulent velocity fluctuations on individual particle trajectories by introducing stochastic perturbations based on the turbulence characteristics of the continuous phase (ANSYS, 2012).

Despite their advantages, stochastic models such as DRW and CRW exhibit several notable limitations. First, they rely on simplified representations of turbulence, typically

modeling turbulent eddies as isotropic, Gaussian in nature, and possessing fixed lifetimes. This fails to capture coherent structures and anisotropy that are characteristic of real cough jets, often resulting in inaccuracies in droplet trajectory predictions (Lancmanová; Bodnár, 2025).

Second, these models often assume one-way coupling, neglecting the feedback of momentum, energy, and mass from droplets to the carrier phase. This simplification is especially critical in dense cough plumes, where evaporative cooling can significantly influence buoyancy and flow structures, effects that standard DRW and CRW implementations are not designed to capture.

Third, stochastic models frequently treat droplets as non-evaporating and of fixed size, ignoring important dynamic processes such as evaporation, breakup, and coalescence. These processes greatly impact droplet lifetime and transport behavior (Zodo *et al*., 2025). Moreover, model predictions are highly sensitive to uncertain input parameters, including the initial droplet size distributions and emission velocities. These variables are often not constrained by the model itself, which reduces its reliability in quantitative risk assessments (Trivedi *et al*., 2021).

Lastly, stochastic tracking models are commonly coupled with Reynolds-Averaged Navier-Stokes (RANS) turbulence closures. These models, by nature, are unable to resolve small-scale or transient turbulent structures that are essential for accurately capturing the complex dynamics of cough jets. High-fidelity turbulence models such as Large Eddy Simulation (LES) or Direct Numerical Simulation (DNS) provide improved accuracy but require significantly greater computational resources (Norvihoho *et al*., 2023).

In this study, particle dispersion due to turbulence was modeled using the stochastic tracking method. The mean fluid-phase velocity ($\bar{u}$) was obtained from the flow field solution (Equation 15), and particle trajectories were calculated based on the stochastic formulation presented in Equation 19.

$$\vec{u}_g = \bar{u} + u' \tag{19}$$

where u' represents the fluctuating velocity component. Individual particle trajectories are computed by integrating the instantaneous velocity $\bar{u}+u'(t)$ along the trajectory path.

To estimate dispersion, the Lagrangian integral time scale T, which is proportional to the rate of particle dispersion, is applied as shown in Equation 20:

$$T = \int_0^\infty \frac{u_d'(t)\,u_d'(t-\tau)}{\overline{u_d'^2}} \tag{20}$$

A higher value of T indicates stronger turbulence. For small tracer particles that follow the flow field, the Lagrangian time scale T_L within the SST k-ω is approximated by Equation 21:

$$T_L \approx \frac{0.30}{\omega} \tag{21}$$

In the Discrete Random Walk, velocity fluctuations u', v' ,w' are defined as Gaussian random variables derived from the Reynolds-averaged Navier-Stokes (RANS) simulations, as given in Equation 22:

$$\left(u',v',w'\right)= \zeta R \tag{22}$$

Where ζ and R are normally distributed random variables with zero mean and unit variance. The random velocity components are updated over a time interval equivalent to the eddy lifetime, defined in Equation 23:

$$\tau_e = 2T_L \tag{23}$$

It is assumed that particles interact with the fluid phase over a minimum eddy lifetime or an eddy crossing time, as defined by Equation 24:

$$t_{interaction} = f\left(\tau_e,\ t_{cross}\right) \tag{24}$$

The eddy crossing time, t_{cross}, is calculated by Equation 25:

$$t_{cross} = -\ \tau_d \ln \ln \left[1-\left(\frac{L_e}{\tau_d\left|\vec{u}_i-\vec{u}_d\right|}\right)\right] \tag{25}$$

Here, τ_d is the particle relaxation time, L is the eddy length scale, and $\left|\vec{u}_i-\vec{u}_d\right|$ is the magnitude of the relative velocity between the eddy and the particle.

The relaxation time τ_d and eddy length scale L_e are given by:

$$\tau_d = \frac{1}{18}\ \frac{\rho_d S d_d^2 C_c}{\mu_d} \tag{26}$$

$$L_e = \tau_e\sqrt{\frac{2k}{3}} \tag{27}$$

where S is the density ratio, and C_c is the Cunningham slip correction factor, defined by Equation 28:

$$C_c = 1+\frac{2\lambda}{d_d}\left[0.4\,e^{-\left(\frac{1.1d_d}{2\lambda}\right)}+1.25\right] \tag{28}$$

with λ representing the mean free path of the droplets, once the interaction time (Equation 21) is reached, a new velocity is generated using updated ζ values in Equation 22. Additional details regarding the constants employed can be found in ANSYS (2012).

Cough droplets are generally non-uniform upon release (Chao *et al*., 2009; Yan; Li; Tu, 2019). However, in this study, uniform droplet batches were used, each consisting of droplets of a specific size ranging from 1 µm to 100 µm. This approach offers a simplified yet reasonable representation of the size spectrum typically observed in droplets expelled during human coughing.

Using uniform droplet sizes (monodisperse distributions) is justified because it significantly reduces computational costs in droplet-laden CFD simulations, especially when employing the Discrete Phase Model (DPM) in ANSYS Fluent. Choosing monodisperse diameters reduces the number of particles to track, simplifies trajectory calculations, and cuts down CPU time, while still capturing essential flow and dispersion behaviors.

For example, Guerra, Achiles and Béttega (2017) studied liquid dispersion in a Venturi scrubber by comparing simulations based on measured droplet size distributions to those using single-size droplets. Their results showed that the simplified model, though less detailed, was computationally efficient and maintained key dispersion characteristics.

Similarly, Thakur and Murthy (2022), in their research on inkjet droplet formation, used fixed droplet diameters across different nozzle sizes and found that monodisperse configurations enabled "inexpensive, fast, and flexible" simulations of droplet stability in ANSYS Fluent.

Additionally, recent reviews on airborne droplet modeling during the COVID-19 pandemic indicate that, although real aerosol clouds are naturally polydisperse, using representative droplet sizes is a common and acceptable approximation to reduce computational complexity in simulations involving droplet transport and evaporation.

Overall, these findings support the use of uniform droplet sizing in Fluent simulations as a practical approach to minimize particle tracking and source-term calculations, thereby improving computational efficiency without significantly sacrificing accuracy.

2.2.2 Coupling

The selection between one-way and two-way coupling in multiphase flow simulations primarily depends on the volume fraction and mass loading of the dispersed phase, as well as the specific objectives of the study.

One-way coupling is typically appropriate when the particle volume fraction is very low, generally below 10^{-6}, and the mass loading is insufficient to exert a meaningful impact on the flow field of the continuous phase. In such scenarios, particles or droplets are influenced by the fluid, but do not provide feedback to it. This results in reduced computational requirements, making the approach suitable for simulations involving low-concentration environments, such as aerosol transport or dilute particle dispersion (Elghannay; Tafti, 2018).

Conversely, two-way coupling becomes necessary when the volume fraction exceeds approximately 10^{-6}, or when the mass loading surpasses 10^{-3}. Under these conditions, the feedback from the dispersed phase on the continuous phase, affecting parameters such as velocity, temperature, and turbulence, can no longer be neglected.

Recent studies, including that of Tom, Carbone and Bragg (2022) have demonstrated that even with mass fractions as low as 7.5×10^{-3}, particles can significantly modify the

flow field, influencing mechanisms such as deposition and sedimentation. In applications involving dense sprays, fluidized beds, or pneumatic conveying systems, where interaction between phases is critical, two-way coupling is essential for ensuring result fidelity (Bhattacharjee *et al*., 2024; Wu *et al*., 2024).

Therefore, the decision between coupling strategies must consider the physical characteristics of the system and strike a balance between desired simulation accuracy and computational cost.

3 Numerical set-up

The numerical simulations were performed using ANSYS Fluent 14.5. For pressure-velocity coupling, Fluent provides five algorithms: the Semi-Implicit Method for Pressure-Linked Equations (SIMPLE), SIMPLE-Consistent (SIMPLEC), Pressure-Implicit with Splitting of Operators (PISO), Coupled, and Non-Iterative Time Advancement (NITA). These algorithms are commonly used to solve the Navier-Stokes equations in CFD.

In the present study, the SIMPLE algorithm was employed due to its fundamental and stable characteristics. This method is categorized as a segregated solver and resolves the governing equations of fluid flow by utilizing the relationship between velocity and pressure corrections. Further details regarding the SIMPLE algorithm can be found in Patankar (1980).

For spatial discretization, the Second-Order Upwind scheme was applied to the momentum, turbulent kinetic energy, specific dissipation rate, energy, and species (water and air) equations. This scheme is particularly suitable for problems involving strong convective terms, turbulence, and species transport, as it enhances solution accuracy by employing gradient-based extrapolation from upstream cells. A comprehensive description of this scheme is available in Shyy, Thakur and Wright (1992).

For the transient formulation, the Second-Order Implicit scheme was adopted. This time discretization method ensures second-order temporal accuracy, which is advantageous for simulations requiring precise resolution of transient phenomena. Being implicit, the method relies on iterative solution procedures with unknown variables evaluated at the future time level. Further explanation of this formulation can be found in ANSYS (2012).

Time step sizes ranged from 10^{-3} s to 10^{-5} s. Specifically, a time step of 10^{-3} s was utilized for simulating larger droplets (50 μm and 100 μm), while 10^{-5} s was employed for smaller particles (1 μm and 10 μm). The use of different time steps is justified by the faster evaporation rates of smaller droplets, which necessitate more refined time resolution for accurate calculation of heat, mass, and momentum exchange. Conversely, the flow behavior of larger droplets could be resolved with comparatively coarser time steps.

The scaled residuals for the discrete phase (water droplets) converged to a tolerance of 10^{-12}, while the energy residual reached 10^{-14}, values that fall within the recommended range of the ANSYS Fluent User's Guide (ANSYS, 2012). Although residual plots are not definitive indicators of convergence in transient simulations, ANSYS (2012) advises that the time step be sufficiently small to achieve a reduction of at least three orders of magnitude in solution residuals within a single time step. This criterion was satisfied in the present simulations.

3.1 Geometry and mesh

To replicate and simulate human cough dynamics, a computational domain measuring 2.5 m × 1 m × 2.5 m was constructed (Figure 1). The cough inlet (mouth region) was positioned 1.70 m above the ground level. Given the geometric complexity of the human mouth and its impact on computational cost, a simplified quadrilateral inlet with an area of 4 cm² was modeled, as similarly implemented by Li *et al*. (2020), D'Alessandro *et al*. (2021) and Ge *at al*. (2022). The inlet surface begins at x = -0.02 m and intersects the cough chamber at x = 0.00 m. Accordingly, results along the x-axis are reported beginning from negative x-values, progressing into the positive axis.

Figure 1 ▼
3D cough chamber.
Source: elaborated by the authors

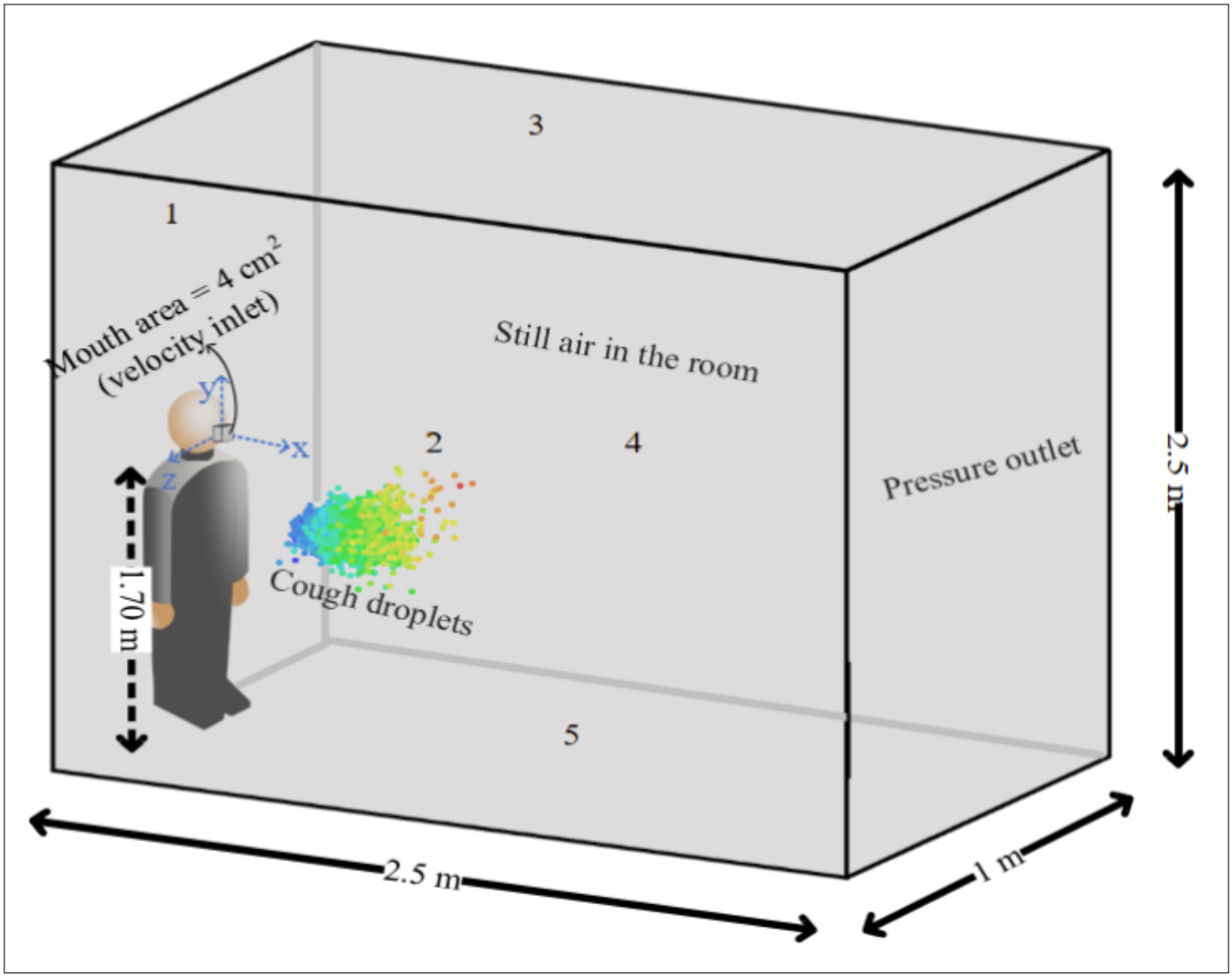

The computational domain was meshed using ANSYS Meshing 14.5, applying unstructured tetrahedral elements. Mesh refinement was increased near the inlet region (using a total of 3,200 cells) to enhance solution accuracy in this area (Ayuba; Justi; Lopes, 2025). Figure 2 provides a visual representation of the graded mesh. Further mesh characteristics and the convergence test are detailed in subsection 4.1, where labels A, B, and C denote the inlet, walls, and outlet boundaries, respectively.

ISSN 2447-9187

Figure 2 ▶
Visual representation of graded tetrahedral mesh and boundary conditions.
Source: elaborated by the authors

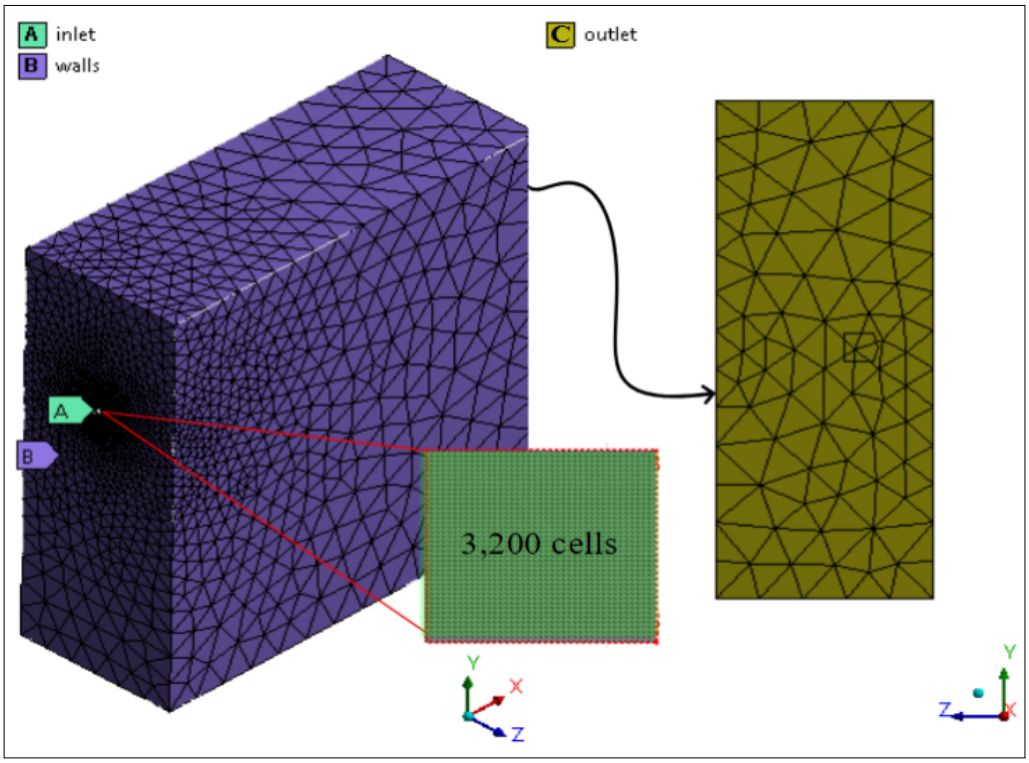

In the DPM framework, each computational cell represents a droplet; therefore, the 3,200 cells depicted in Figure 2 correspond to the number of particles injected into the cough chamber per time step. The same surface was also configured for injecting humid air (continuous phase), with additional details provided in subsection 3.2.

3.2 Initial and boundary conditions

The influence of shear rate on cough droplets is negligible (Dbouk; Drikakis, 2020; Van Der Reijden; Veerman; Amerongen, 1993). Consequently, the physical properties of pure water, available in the Fluent material database, were adopted to represent the cough droplets simulated in this study.

At the inlet, the airflow velocity profile corresponding to a human cough was defined using the curve presented by Li *et al*. (2020), as shown in Figure 3. In this model, particles were introduced into the domain with a velocity reaching a maximum of 10 m/s for 0.12 seconds. The total duration of the simulated cough was 0.52 seconds.

Figure 3 ▶
Air inflow velocity profile representing a single cough based on Li *et al.* (2020) and applied in this work.
Source: research data

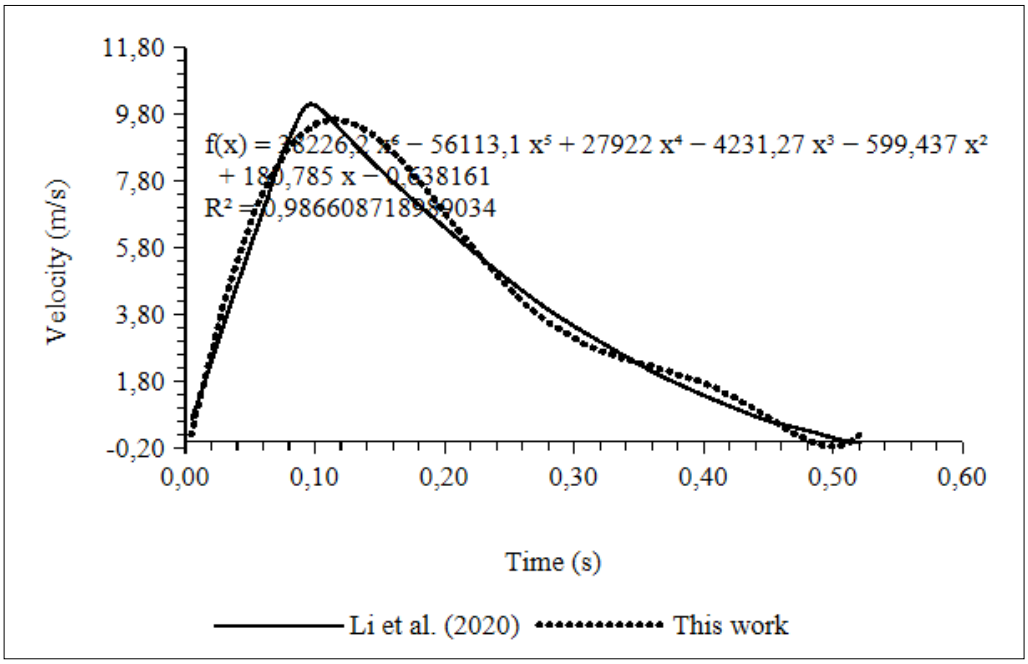

To ensure particles remained within the computational domain, either until reaching the floor (in the case of heavier droplets under high-humidity conditions) or until complete evaporation (for smaller droplets), a "reflect" boundary condition was applied at the inlet (A) and wall surfaces (B). This condition enables particles to rebound upon contact with these surfaces, with momentum adjustments based on the coefficient of restitution, defined as $\xi_n = v_{2,n} / v_{1,n}$, are the normal components of particle velocity before and after collision, respectively. This prevents droplets from artificially disappearing upon contact with walls.

At the outlet boundary (C), an "escape" condition was applied. Under this condition, particles are removed from the simulation domain upon contact with the outlet surface, and their mass, energy, and momentum calculations are terminated accordingly.

The entire cough chamber and its boundaries were maintained at a constant temperature of 293.15 K.

To specify the relative humidity at the inlet and throughout the computational domain (Figure 1), the commercial software required the definition of the water vapor mass fraction. Assuming the continuous phase behaves as an ideal gas, the mass of water vapor M_v can be calculated using the equation of state, as show in Equation 29 (Cengel; Boles, 2015):

$$M_v = MW_v \frac{PV}{RT} = MW_v \; n_v \tag{29}$$

where MW_v is the molecular weight of water vapor (in g/mol), P is the pressure (in atm), V is the volume (in m^3), R is the universal gas constant (in J/mol.K), T is the temperature (in K), and n_v is the number of moles.

The molecular weight of the continuous phase mixture is a function of its components, i.e., dry air and water vapor, and can be calculated by:

$$MW_g = MW_a \cdot y_a + MW_v \cdot y_v \tag{30}$$

where MW_a = 29 g/mol is the molecular weight of dry air, and y_a and y_v are the mole fractions of air and vapor, respectively.

The relative humidity (RH_i) of an ideal air-vapor mixture at given temperature can be expressed as:

$$RH_i = \frac{P_i}{P_i^*} x \ 100\% \tag{31}$$

where P_i is the vapor pressure and P_i* is the saturated vapor pressure of the mixture. Since the domain temperature was set at 293.15 K in all simulations, P_i was obtained from the steam table at the saturation temperature (373.12 K), as described by Cengel and Boles (2015). This vapor mole fraction (y_w) was then determined as follow:

$$y_w = \frac{P_i}{P_{total}} \tag{32}$$

with P_{total} representing the ambient pressure. Given that $y_w + y_a = 1$, the mass fraction of vapor (MW_g) can be calculated.

Figure 4 presents the correlation between vapor mass fraction and relative humidity under the conditions adopted in this study. This relationship was used to assign the appropriate mass fraction value to the cell zone via Fluent's "patch" function.

Figure 4 ▶
Relationship between vapor mass fraction of pure water and relative humidity at 293.15 K and 1 atm adopted in this study.
Source: elaborated by the authors

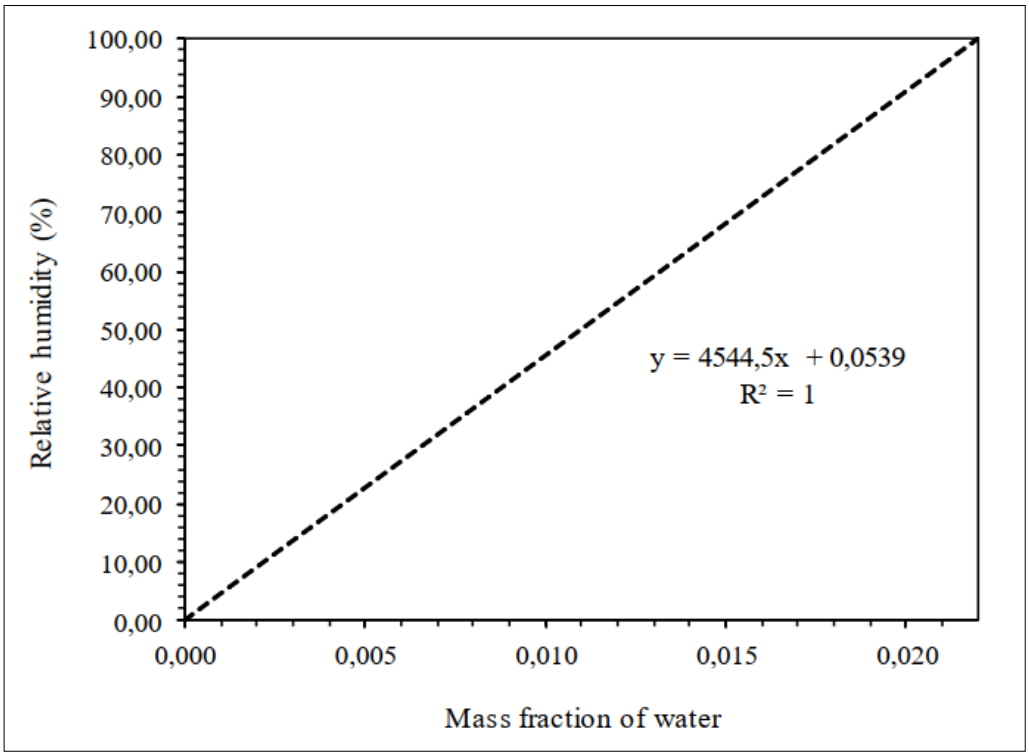

In this study, droplets were released at saturated vapor pressure (RH = 100%), following the approach proposed by Li *et al*. (2020). For the domain environment, two relative humidity (RH) levels were tested: 0% and 80%. These RH values were selected to represent two extreme environmental scenarios, extremely dry and highly humid, enabling assessment of their impact on cough jet behavior.

Although a 0% RH condition is rare in real-world situations, it serves as a theoretical extreme for investigating maximum evaporation. In contrast, the 80% RH condition

reflects realistic indoor or tropical environments, where droplet evaporation is significantly slower. Similar ranges have been adopted in previous CFD studies, including those by Aliabadi *et al*. (2010) and Wang, Zeng and Yan (2024).

To establish the desired RH conditions within the cough chamber, the "patch" function (ANSYS, 2012) was used to initialize the mass fractions corresponding to each relative humidity level. This function allows the assignment of initial field values, in this case, mass fraction, to conduct transient simulations (Figure 4).

3.3 Simulated cases

At this stage, two computational models, M1 and M2, were utilized to represent one-way and two-way coupling, respectively, as discussed in subsection 2.2.2. These models were employed to examine the impact of droplet diameter and ambient relative humidity on the dispersal of contaminated droplets released during intense respiratory events.

In the one-way coupling model, the continuous phase influences the discrete phase in terms of mass, energy, and momentum transfer. Conversely, in the two-way coupling model, interactions occur bidirectionally, allowing the discrete phase also to affect the continuous phase.

The relative humidity levels of the computational domain and the droplet diameters utilized in the simulations are presented in Table 1. The combinations of relative humidity and droplet sizes are categorized into Cases 1 through 8.

Table 1 ▶
Simulated cases with corresponding relative humidity and droplet diameters used in this study.
Source: research data

Relative humidity (%)	**Droplet diameter (µm)**			
	1	10	50	100
0	Case 1	Case 3	Case 5	Case 7
80	Case 2	Case 4	Case 6	Case 8

Additionally, key simulation parameters such as flow rate, inlet area, temperatures, emitter height, and the range of droplet diameters were adapted from Li *et al*. (2018) and Li *et al*. (2020). These parameters are summarized in Table 2.

Table 2 ▶
Simulation parameters adapted from Li *et al*. (2020) and applied in this study.
Source: research data

Parameter	**Value / description**
Flow rate	1.80×10^{-5} kg/s
Species	Air and water
Cougher's mouth areas	4 cm^2
Cough temperature	310.15 K
Room temperature	293.15 K
Cougher's height	1.70 m
Droplet diameter	1 µm, 10 µm, 50 µm, 100 µm

A square-inlet geometry was used to represent the mouth. Even though such simplification affects precision in the flow direction and dispersion, it has a computational

cost advantage. In the same direction, a rectangular inlet has been applied in the work of Chillón *et al*. (2024) and D'Alessandro *et al*. (2021), a circular one has been used in the work of Oh *et al*. (2022), Li *et al*. (2018) and Redrow *et al*. (2011), a squared inlet has been used by Gupta, Lin and Chen (2009) and Pan *et al*. (2022), and lastly, ellipse has been applied in the work of Oh *et al*. (2022). The use of simple geometries makes meshing more convenient at the domain inlet, since relatively coarser cells can be applied (Cao *et al*., 2022).

3.4 Mesh independence test

In CFD, mesh independence studies are crucial to confirm that simulation results are not affected by the numerical discretization of the domain. This process involves solving the same physical problem using increasingly refined meshes and comparing key variables such as velocity, pressure, temperature, and, in this case, droplet diameter, until changes between successive refinements become negligible.

Mesh independence signifies that the numerical solution has converged with respect to mesh size, meaning further refinements do not significantly alter the results. This improves the reliability of the simulated data, ensuring that observed trends stem from the physical modeling rather than numerical artifacts (Versteeg; Malalasekera, 2007; Roache, 1998). Therefore, mesh independence studies are an essential step in numerical verification, enabling a balance between computational cost and result accuracy in CFD simulations.

To perform the simulations, a mesh independence test was conducted using three different mesh sizes (G1 < G2 < G3), as detailed in Table 3. All meshes were generated with a growth rate of 1.10 and a minimum element length of 5.0×10^{-5} m. The maximum element size in each case was determined according to the geometric progression presented in Equation 33:

$$a_n = a_1 \cdot r^{n-1} + a_1 \tag{33}$$

where a_1 corresponds to the maximum element size of *G1*, n is the index of the mesh in the sequence, and r is the common ratio (e.g., $r = l_{G2} / l_{G1}$), where l_{G1} and l_{G2} are the respective element sizes of meshes *G1* and *G2*). It is worth noting that reducing the maximum element length leads to finer meshes with higher element density, especially near the inlet region. The selected mesh size distribution allows a wide range of maximum element lengths. Details of the three meshes are provided in Table 3.

Table 3 ▶
Parameters of the three-dimensional numerical meshes with varying element sizes.
Source: research data

Mesh parameters	G1	G2	G3
Minimum cell volume ($\times 10^{-12}$ m^3)	5.18	5.08	3.62
Maximum cell volume (m^3)	5.31×10^{-2}	1.96×10^{-3}	1.32×10^{-4}
Number of nodes	41,349	42,145	56,162
Number of elements	229,253	233,327	309,908
Av. skewness	0.23	0.23	0.23

In numerical modeling and simulation, the quality of the results is directly influenced by the mesh used. One of the key indicators of mesh quality is skewness. Highly skewed elements reduce the accuracy of the solution, so it is recommended to maintain skewness values between 0 and 0.5 (Santana *et al*., 2020). Additionally, ANSYS (2012) suggests maintaining an average skewness below 0.33, which is consistent with the values used in this study.

The mesh convergence analysis was conducted by injecting 3,200 particles with a diameter of 100 µm at a velocity of 10 m/s, under the operating conditions presented in Table 2. The test evaluated droplet evaporation and velocity outcomes using the three mesh configurations, as detailed in subsection 3.4.1.

3.4.1 Droplet evaporation

Figure 5 shows the evaporation behavior of 3,200 cough droplets after 5 seconds of simulation time (based on conditions from Table 2), using the three meshes described in Table 3 and under the two-way coupling model (M2) presented in Table 1.

Figure 5 ▶
Evaporation of 3,200 droplets over 5 seconds of simulation time using three meshes with different refinements.
Source: research data

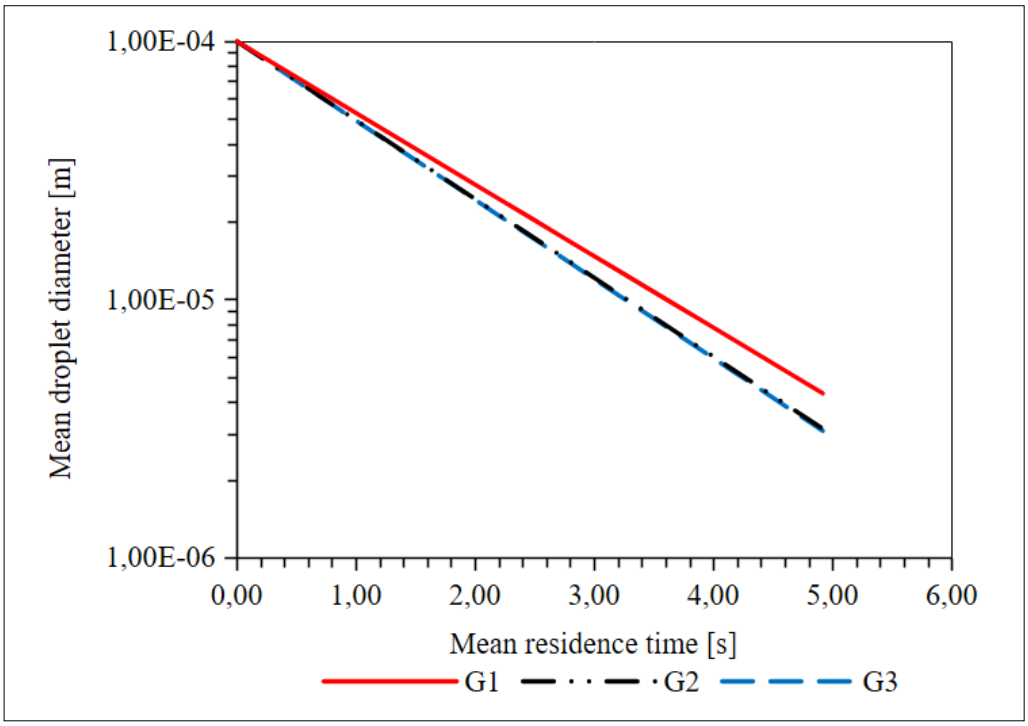

After 5 seconds, similar mean droplet diameters were observed for meshes G2 (3.16×10^{-6} m) and G3 (3.24×10^{-6} m), while G1, the coarsest mesh, produced a significantly larger average diameter (4.35×10^{-6} m). Since further mesh refinement did not substantially alter the results, mesh independence was considered achieved, an approach similar to that employed by Bahramian, Mohammadi, and Ahmadi (2023).

3.4.2 Mesh selection

Figure 6 ▼
Mesh structure and skewness distribution for G2, representing the quality of tetrahedral elements.
Source: research data

Based on the droplet evaporation analysis, mesh G2 was selected due to its balance between computational cost and accuracy, as recommended by Bahramian, Mohammadi, and Ahmadi (2023). The results obtained with G2 were comparable to those with G3, while G2 was approximately 58% more computationally efficient. The mesh composition and skewness distribution for G2 are presented in Figure 6.

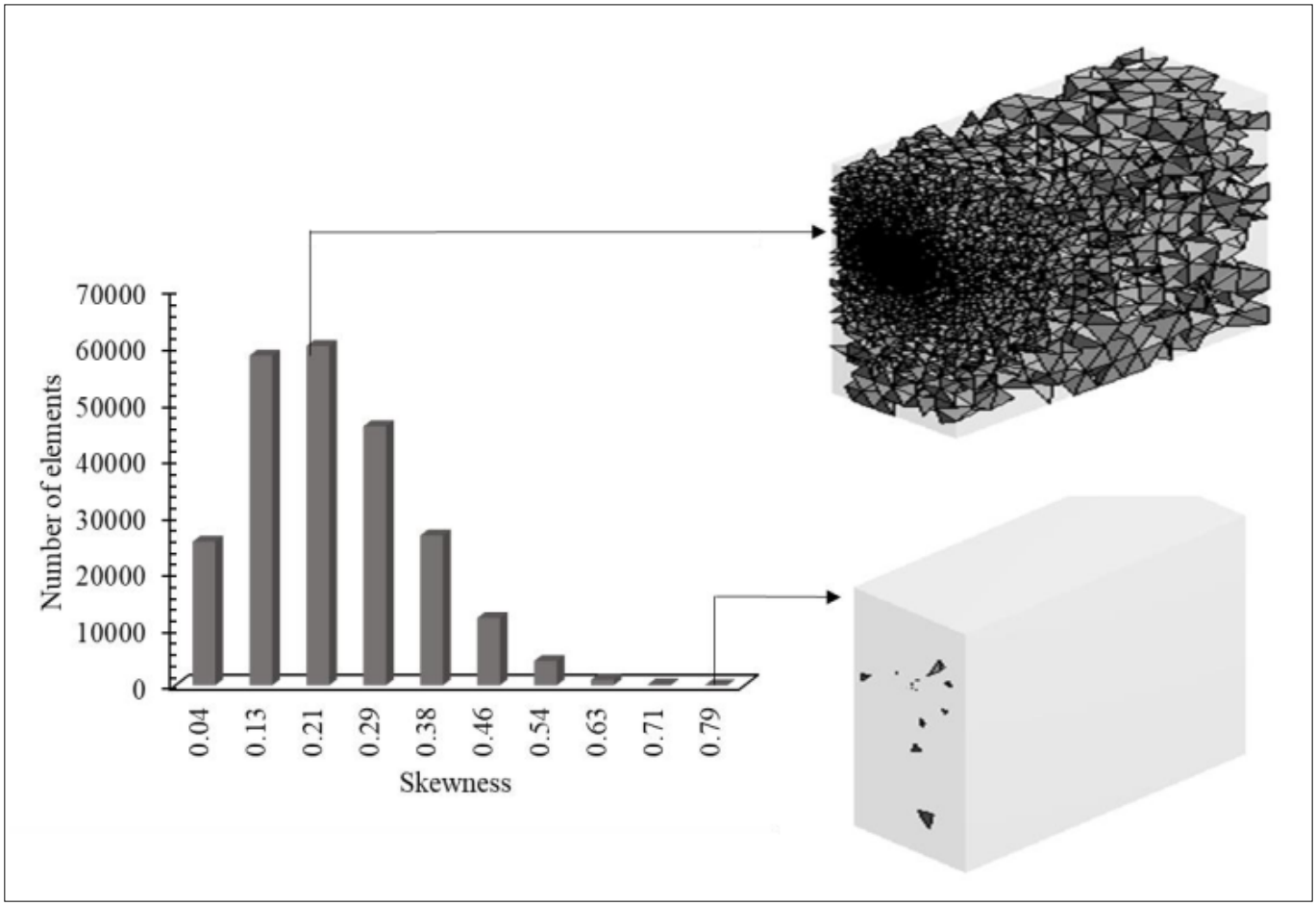

As shown in Figure 6, the skewness in the mouth region was low (between 0.04 and 0.13), with most mesh elements exhibiting skewness values below 0.5. This indicates good mesh quality and suggests that the simulation results obtained with this mesh are reliable. Specifically, mesh G2 presented minimum, maximum, and average skewness values of 1.28×10^{-3}, 0.83, and 0.23, respectively, all within acceptable limits according to Santana *et al*. (2020).

3.4.3 Comparison with literature results

Mesh G2 and model M2 were employed to simulate the behavior of a single droplet and to compare the results with those reported by Li *et al*. (2020), under the same operating conditions (Table 2). The referenced authors analyzed three droplet

Figure 7 ▼
Evaporation of cough droplets of different sizes in a quiescent room at 0% relative humidity.
Source: research data

diameters (1 µm, 10 µm, and 100 µm) in a quiescent room environment under different relative humidity conditions.

In this study, simulations were conducted under 0% relative humidity, one of the scenarios used by Li *et al*. (2020), using the same droplet diameters. To enable the comparison, the mean droplet diameter after the evaporation of 3,200 droplets was calculated. The results are presented in Figure 7.

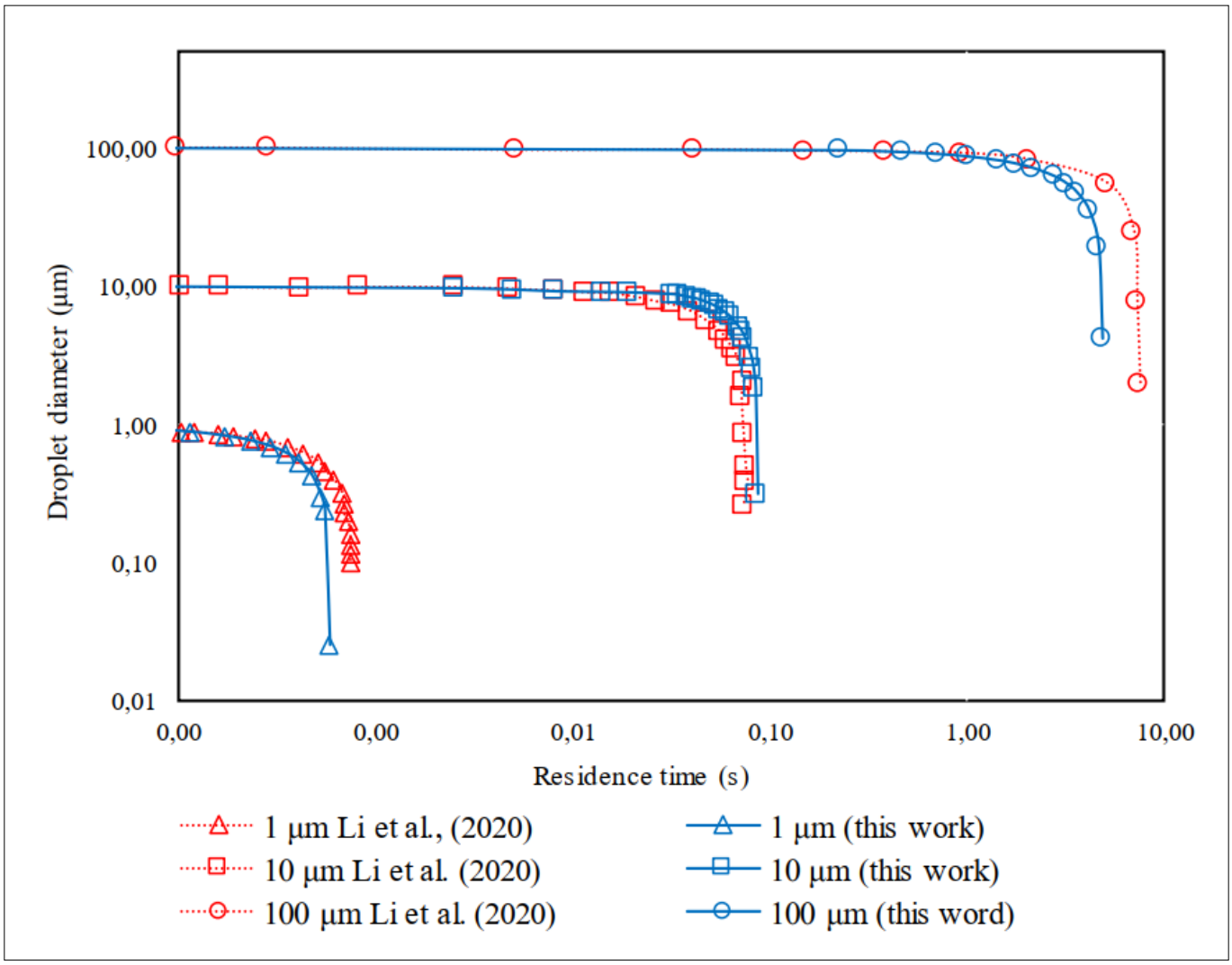

Although Li *et al*. (2020) investigated the behavior of single droplets, and the present study considered 3,200 particles, the results were found to be comparable. The tests demonstrated that the selected mesh configuration was capable of solving the flow problems addressed in this study with a high degree of precision, convergence, and stability, while also providing a considerable advantage in computational time.

4 Results and discussion

The simulation cases are presented and discussed in pairs. The coupling models applied in this study were evaluated under two relative humidity conditions (0% and 80%) and four droplet diameters (1 µm, 10 µm, 50 µm, and 100 µm). For

each scenario, 3,200 droplets were released in a single time step, and the mean droplet diameter was calculated. Droplet trajectories were tracked at specific time intervals. In the following subsections, the effects of phase coupling, humidity, and droplet size are analyzed. Model M1 refers to one-way coupling, while Model M2 refers to two-way coupling.

4.1 Cases 1 and 2

Table 4 ▼
Horizontal distance traveled by 1 µm droplets under different coupling models and humidity conditions.
Source: research data

These represent the first set of simulations conducted in this study. The particles have a diameter of 1 µm, and the simulations were performed under 0% (Case 1) and 80% (Case 2) relative humidity conditions. The results are presented in terms of the horizontal distances traveled by the respiratory droplets, as shown in Table 4.

	Case 1		Case 2	
Model	**Horizontal distance (m)**	**Standard deviation**	**Horizontal distance (m)**	**Standard deviation**
M1	3.47×10^{-5}	4.66×10^{-6}	3.65×10^{-5}	2.03×10^{-6}
M2	3.46×10^{-5}	3.56×10^{-6}	6.75×10^{-5}	7.88×10^{-5}

Cough droplets traveled relatively short horizontal distances before complete evaporation, effectively evaporating almost immediately upon release. In Case 1, the horizontal distances predicted by M1 and M2 showed only minor discrepancies. In Case 2, however, a more pronounced difference was observed, particularly under M2. This can be attributed to the higher relative humidity level (80%), which reduces the vapor pressure gradient between the droplet surface and the surrounding air. Consequently, the evaporation rate decreases, allowing droplets to persist longer in liquid form and travel greater horizontal distances before fully evaporating.

The low standard deviations observed across all scenarios indicate that the droplets remained clustered around the mean horizontal displacement. Based on the results presented in Table 4, it can be concluded that the coupling model had a negligible influence on droplet behavior, whereas relative humidity had a more substantial impact on evaporation dynamics.

4.2 Cases 3 and 4

Cases 3 and 4 comprise the second simulation set. These cases employed a 10 µm particle diameter at 0% (Case 3) and 80% (Case 4) relative humidity. The results are presented as droplet travel distances (horizontal and vertical) over time and as particle cloud distributions, as shown in Figure 8. The mean diameter of the particle cloud was analyzed at different time intervals to generate the curves in subfigures (a) and (b).

Figure 8 ▶
Droplet travel and cloud dispersion for 10 µm particles under different humidity conditions. (a) Horizontal displacement; (b) Vertical displacement; (c) Particle cloud dispersion at t = 0.10 s for Case 4 – Model M2 (color scale indicates distance along x-axis).
Source: research data

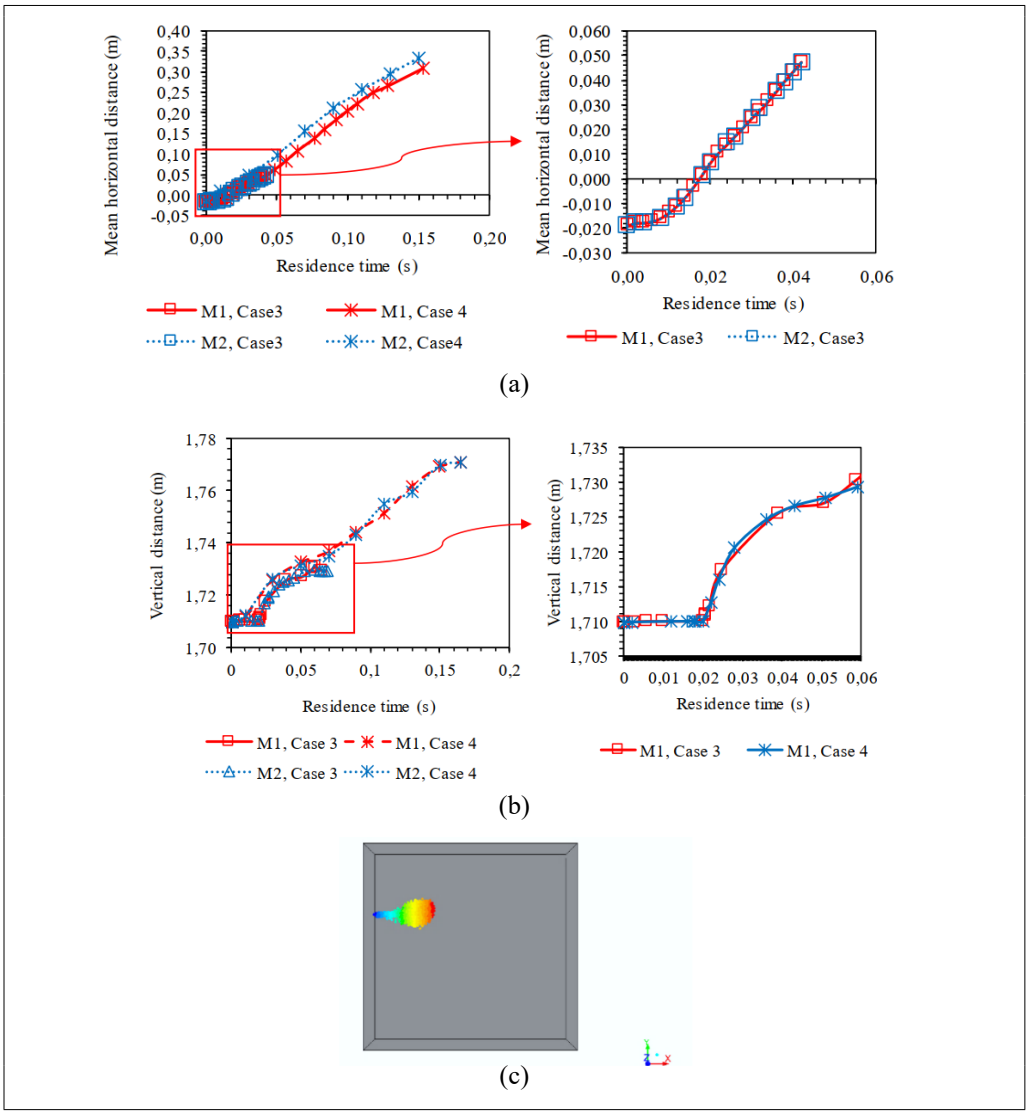

For Case 3, both models M1 and M2 yielded similar results for horizontal and vertical displacement, indicating that the discrete phase had little influence on the continuous phase. In Case 4, a slight difference was observed between M1 and M2 in horizontal displacement; at 0.15 seconds, M1 predicted 0.31 m, whereas M2 predicted 0.33 m. The particle cloud initially expanded symmetrically in the x, y, and z directions. In Figure 8c, the color grading represents the extent of this dispersion: blue, green, and red correspond to short, medium, and long travel distances, respectively.

For both models in Case 3, particle evaporation began at approximately 0.042 seconds, with the maximum horizontal distance reaching 0.047 m. Vertically, the particles reached 0.030 m above the cough level. In contrast, the cloud in Case 4 reached a vertical distance of 0.07 m, representing an 80% increase over Case 3 due to higher ambient humidity.

These results show that Cases 1 through 4, characterized by small respiratory droplets, involved droplets that traveled insignificant distances regardless of humidity. This suggests they may not qualify as contagious respiratory droplets under the tested conditions. However, this study evaluates droplet behavior only until evaporation, which presents a limitation.

Other studies, such as those by Dhand and Li (2020) and Li *et al.* (2020), have shown that cough droplets may persist in the form of aerosols even after water content evaporates, due to the presence of non-volatile substances such as DNA and salts. In such cases, distance cannot

be reliably measured since particles continue to float and may travel long distances. Therefore, for effective control of aerosol-based IRD transmission, proper ventilation and the use of face masks are recommended (Wu *et al*., 2024).

4.3 Cases 5 and 6

The third group of simulations was conducted for Cases 5 and 6, under relative humidity conditions of 0% and 80%, respectively, using particles with a diameter of 50 µm. The results are presented in Figure 9 (next page).

Figure 9 ▶
Horizontal and vertical displacement of 50 µm droplets simulated by Models 1 and 2 under 0% and 80% relative humidity: (a) horizontal trajectory; (b) vertical trajectory; (c) Case 6 (Model 2) particle cloud formation at t = 0.10 s. Color gradient represents particle cloud propagation along the x-axis, from blue (shorter distance) to red (longer distance).
Source: research data

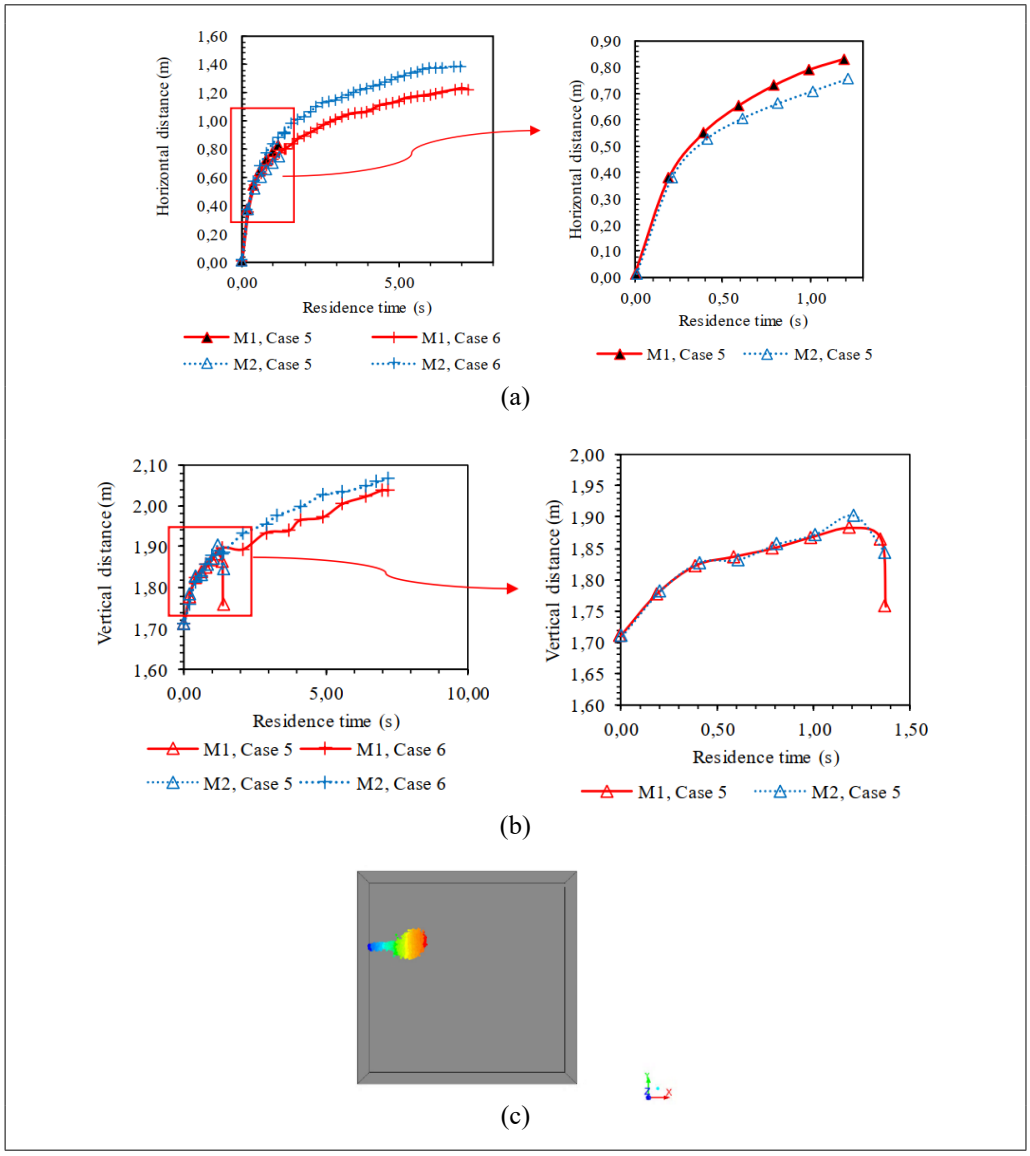

As in the analysis presented in subsection 4.2.2, the results are shown as horizontal and vertical displacement versus time, along with visual representations of the particle cloud.

In Case 5, the horizontal distance reached by the droplets differed slightly between the models. Model 2 (M2) calculated a horizontal displacement of $x = 0.72$ m, whereas Model 1 (M1) estimated $x = 0.81$ m at $t = 1.19$ s. In Case 6, M1 predicted $x = 1.24$ m and M2, $x = 1.34$ m at $t = 7.00$ s.

A more detailed analysis reveals that although the droplets in Cases 5 and 6 are larger than those in Cases 3 and 4, the particle clouds formed (Figure 9c) were similar for both M1 and M2. In Case 5, evaporation began at 1.19 s and 1.21 s for M1 and M2, respectively. At these times, horizontal and vertical displacements were 0.83 m and 0.76 m, and 0.18 m and 0.14 m, respectively.

In Case 6, the droplets persisted longer before evaporating, due to the increased relative humidity. Compared with Case 5, the onset of evaporation was delayed by approximately 142%, while the maximum horizontal distance increased by more than 30%.

It is noteworthy that the 50 µm droplets in both cases descended to approximately one-quarter of the emitter's height (1.70 m) before fully evaporating.

In this study, 50 µm droplets are classified as "medium respiratory droplets". Based on the results, it can be inferred that under conditions of high relative humidity, droplets of this size may remain airborne for longer periods.

4.4 Cases 7 and 8

This final group of simulations corresponds to Cases 7 and 8, conducted under relative humidity levels of 0% and 80%, respectively, using a droplet diameter of 100 µm. The results are presented in terms of horizontal and vertical displacement over time. Graphical representations are provided in Figure 10.

Figure 10 ▶
Displacement of 100 µm droplets in Models 1 and 2 under 0% and 80% relative humidity: (a) horizontal trajectory; (b) vertical trajectory; (c) Case 8 (Model 2) particle cloud at t = 0.10 s (left) and t = 10.00 s (right).
Source: research data

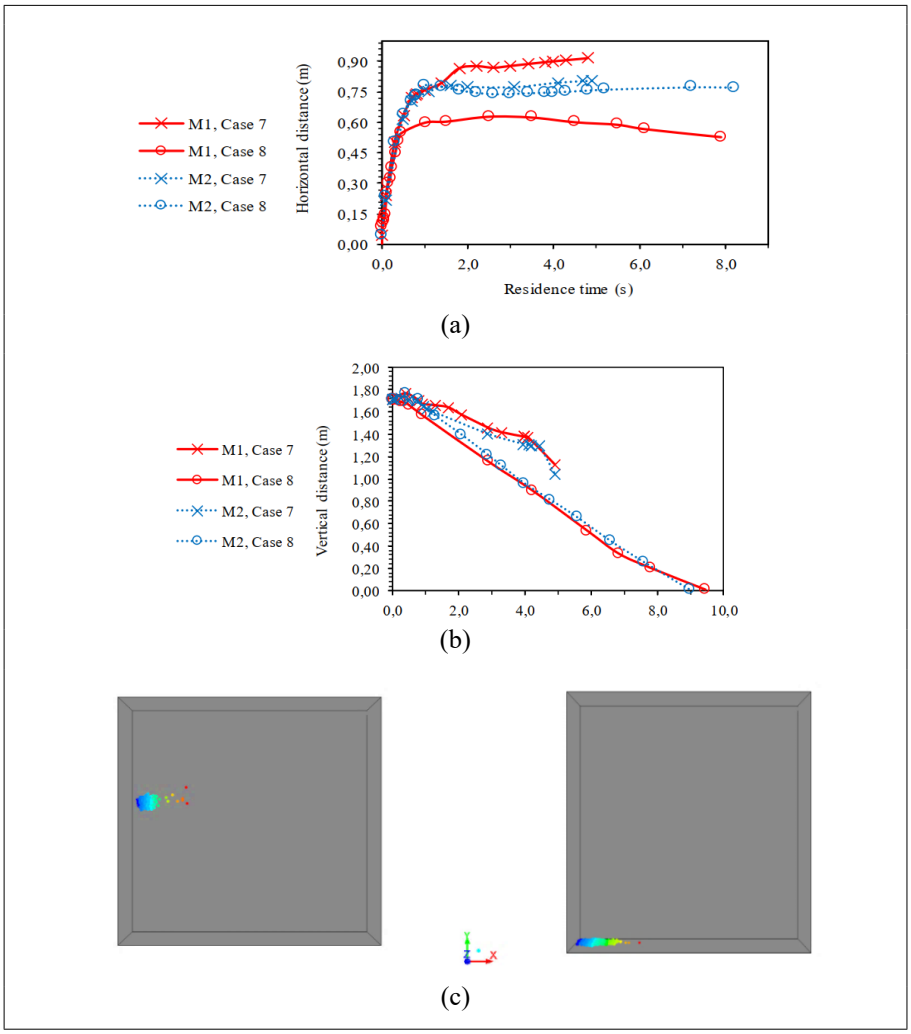

In Case 7, M1 and M2 calculated similar horizontal displacements between $t = 0$ s and $t = 0.99$ s, during which inertial forces predominated and influenced horizontal motion. By $t = 2.00$ s, inertial effects diminished, and gravitational forces prevailed, causing the droplets to fall vertically until evaporation (Case 7) or deposition at the bottom of the domain (Case 8).

The horizontal and vertical distances calculated by M1 and M2 in Case 7 (Figure 10a) were slightly different. M1 estimated a maximum horizontal distance of 0.92 m, while M2 predicted 0.81 m at $t = 4.88$ s. The maximum vertical heights reached were 1.77 m (M1) and 1.73 m (M2).

In Case 8, the horizontal displacements calculated by M1 and M2 were also slightly different: 0.63 m and 0.78 m, respectively. The corresponding maximum vertical displacements were 1.71 m and 1.77 m. This is the only case in which the droplets completed their flow trajectory without fully evaporating, as shown in Figure 10c. The calculated time of flight was 9.46 s (M1) and 8.98 s (M2).

In this study, 100 µm droplets are considered "large respiratory droplets". These droplets tend to fall quickly to the ground, making them less likely to remain airborne. However, they contribute significantly to surface contamination.

Environmental factors, particularly the relative humidity of the coughing environment, play a critical role in droplet behavior. This study found that droplets traveled longer horizontal distances under high humidity (80%) compared to dry conditions (0%), particularly in Cases 2 and 4. Therefore, higher relative humidity increases the likelihood of infectious respiratory droplet (IRD) transmission in enclosed spaces.

Supporting this finding, Auler *et al*. (2020) reported that tropical climates with a relative humidity of 79.6% and a temperature of 27.3 °C favored the spread of COVID-19. Their linear regression analysis revealed a positive correlation between absolute humidity and the COVID-19 transmission rate in some of Brazil's hottest cities, such as Manaus and Fortaleza. Under such environmental conditions, respiratory droplets take longer to evaporate, thereby increasing the risk of IRD transmission through droplets that remain suspended in the air.

Particle diameter is another key factor affecting IRD dispersion, with its influence modulated by the surrounding relative humidity. For example, in Case 6, the longest horizontal distance observed in the study (1.34 m, M2) illustrates the significant effect of high humidity on droplet behavior.

Finally, the coupling phase had a minor influence on the distance travelled by the droplets in both horizontal and vertical directions. However, given the complexity of respiratory fluid dynamics, these differences are not deemed significant. Considering the computational cost of coupling, the uncoupled model is recommended for future simulations in this context.

5 Conclusions

Based on the results obtained, it can be concluded that, although relative humidity (RH) is a significant factor in the dispersion of infectious respiratory droplets (IRDs), the droplets must fall within a specific diameter range to resist both evaporation and gravitational settling, two key factors influencing droplet behavior in enclosed and quiescent environments.

The analysis suggests that medium-sized droplets containing IRDs, when released in a confined space with high relative humidity, are more likely to contribute to contamination. For example, 50 µm droplets under 80% RH traveled a horizontal distance of 1.34 m, the longest distance observed in this study. Therefore, maintaining a minimum physical distance of 1.40 m from potentially infected individuals is recommended to minimize the risk of contamination. Under any RH condition, smaller droplets tend to evaporate rapidly, while larger droplets descend to the ground more quickly, thereby reducing their potential to remain airborne. Nonetheless, it is important to note that large droplets pose a considerable risk of surface contamination.

Although minor differences were observed between the results obtained using the coupling models M1 and M2, both approaches produced similar outcomes regardless of droplet size or relative humidity. Nevertheless, the existing literature suggests that in scenarios involving a large number of droplets, the application of a coupling strategy may improve result accuracy.

In situations where a high concentration of individuals is present in an enclosed space and droplets are emitted through coughing, the effects of coupling should be considered. In such cases, the mass, energy, and momentum transfer from the discrete phase to the continuous phase may become significant, thereby influencing the dynamics of the flow field.

In summary, the findings of this study may contribute to the formulation of guidelines aimed at mitigating the transmission of IRDs in enclosed, quiescent-air environments. Specifically, maintaining low relative humidity in indoor spaces may help reduce the persistence and spread of cough-generated droplets.

Future studies could enhance the complexity of the simulations by incorporating environmental variables characteristic of Brazilian regions. These include local relative humidity levels, unidirectional and multidirectional airflow, and temperature. Particular attention could be given to northern states such as Amazonas and Pará, which experience high humidity, as well as the semi-arid interior regions of northeastern states like Bahia and Paraíba.

Acknowledgments

The authors would like to express their gratitude to the Coordination and Secretariat of the Graduate Program in Chemical Engineering at the Federal University of São Carlos (UFSCar) for providing the facilities and support necessary to carry out this research. Special thanks are also extended to Dr. Liliana de Luca Xavier Augusto, Dr. Marcela Kotsuka da Silva Camara Bastos, and Dr. Vádila Giovana Guerra Béttega for their contributions to the development of this article.

Funding

This study was financed in part by the Coordenação de Aperfeiçoamento de Pessoal de Nível Superior – Brasil (CAPES) – Finance Code 001.

Declaration of competing interest

The authors declare that there is no conflict of interest regarding this work.

Note

This article is derived from a doctoral thesis in Chemical Engineering at the Federal University of São Carlos (UFSCar), available at: https://hdl.handle.net/20.500.14289/21988.

Data availability

The datasets generated and/or analyzed during the current study are not publicly available due to their large size, which makes uploading to cloud platforms impractical. However, they are available from the corresponding author upon reasonable request.

Author contribution

AYUBA, N.: conceptualization, formal analysis, visualization, original draft writing, and Validation; **JUSTI, G. H.; LOPES, G. C.:** supervision, conceptualization, formal analysis, software, writing (review and editing), and validation. All authors participated in writing, discussing, reading and approving the final version of the article.

References

ALIABADI, A. A.; ROGAK, S. N.; GREEN, S. I.; BARTLETT, K. H. CFD simulation of human coughs and sneezes: a study in droplet dispersion, heat, and mass transfer. *In*: ASME INTERNATIONAL MECHANICAL ENGINEERING CONGRESS AND EXPOSITION, 2010, Vancouver. **Proceedings** [...]. Vancouver: ASME, 2010. p. 1051-1060. DOI: https://doi.org/10.1115/IMECE2010-37331.

ANSYS. **ANSYS meshing user's guide**. Canonsburg: ANSYS, 2012.

AULER, A. C.; CÁSSARO, F. A. M.; SILVA, V. O.; PIRES, L. F. Evidence that high temperatures and intermediate relative humidity might favor the spread of COVID-19 in tropical climate: a case study for the most affected Brazilian cities. **Science of the Total Environment**, v. 729, 139090, 2020. DOI: https://doi.org/10.1016/j.scitotenv.2020.139090.

AYTOGAN, H; AYINTAP, E.; YILMAZ, N. Ö. Detection of coronavirus disease 2019 viral material on environmental surfaces of an ophthalmology examination room. **JAMA Ophthalmology**, v. 138, n. 9, p. 990-993, 2020. DOI: http://dx.doi.org/10.1001/jamaophthalmol.2020.3154.

AYUBA, N.; JUSTI, G. H.; LOPES, G. C. Numerical study of coughing in indoor environments: comparison between tetrahedral and hexahedral meshes. **Computational and Applied Mathematics**, v. 44, 222, 2025. DOI: https://doi.org/10.1007/s40314-025-03184-0.

AYUBA, N.; LOPES, G. C. Investigation of the influence of turbulence models on cough droplet evaporation: comparing (SST) k-Ω, k-ε, and

Reynolds stress (RSM) turbulence models. *In*: BRAZILIAN TECHNOLOGY SYMPOSIUM, 7., 2021, Campinas. **Proceedings** […]. Cham: Springer International Publishing, 2023. p. 151-162. (Smart Innovation, Systems and Technologies, v. 207). DOI: https://doi.org/10.1007/978-3-031-04435-9_15.

BAHRAMIAN, A.; MOHAMMADI, M.; AHMADI, G. Effect of indoor temperature on the velocity fields and airborne transmission of sneeze droplets: an experimental study and transient CFD modeling. **Science of The Total Environment**, v. 858, Part 2, 159444, 2023. DOI: https://doi.org/10.1016/j.scitotenv.2022.159444.

BAZANT, M. Z.; BUSH, J. W. M. A guideline to limit indoor airborne transmission of COVID-19. **Proceedings of the National Academy of Sciences**, v. 118, n. 17, e2018995118, 2021. DOI: https://doi.org/10.1073/pnas.2018995118.

BHATTACHARJEE, S.; TOM, J.; CARBONE, M.; BRAGG, A. D. Investigating the parametric dependence of the impact of two-way coupling on inertial particle settling in turbulence. **Journal of Fluid Mechanics**, v. 987, A17, 2024. DOI: http://doi.org/10.1017/jfm.2024.322.

BRANCHE, A. R.; FALSEY, A. R. Respiratory syncytial virus infection in older adults: an under-recognized problem. **Drugs & Aging**, v. 32, p. 261-269, 2015. DOI: https://doi.org/10.1007/s40266-015-0258-9.

CAO, Q.; LIU, M.; LI, X.; LIN, C.-H.; WEI, D.; JI, S.; ZHANG, T.; CHEN, Q. Influencing factors in the simulation of airflow and particle transportation in aircraft cabins by CFD. **Building and Environment**, v. 207, 108413, 2022. DOI: https://doi.org/10.1016/j.buildenv.2021.108413.

CENGEL, Y. A.; BOLES, M. A. **Thermodynamics**: an Engineering approach. 8. ed. New York: McGraw-Hill, 2015.

CHAO, C. Y. H.; WAN, M. P.; MORAWSKA, L.; JOHNSON, G. R.; RISTOVSKI, Z. D.; HARGREAVES, M.; MENGERSEN, K.; CORBETT, S.; LI, Y.; XIE, X.; KATOSHEVSKI, D. Characterization of expiration air jets and droplet size distributions immediately at the mouth opening. **Journal of Aerosol Science**, v. 40, n. 2, p. 122-133, 2009. DOI: https://doi.org/10.1016/j.jaerosci.2008.10.003.

CHILLÓN, S. A.; FERNANDEZ-GAMIZ, U.; ZULUETA, E.; UGARTE-ANERO, A.; BLANCO, J. M. Numerical performance of CO_2 accumulation and droplet dispersion from a cough inside a hospital lift under different ventilation strategies. **Scientific Reports**, v. 14, 6843, 2024. DOI: https://doi.org/10.1038/s41598-024-57425-z.

COLE, E. C.; COOK, C. E. Characterization of infectious aerosols in health care facilities: an aid to effective engineering controls and preventive strategies. **American Journal of Infection Control**, v. 26, n. 4, p. 453-464, 1998. DOI: https://doi.org/10.1016/S0196-6553(98)70046-X.

D'ALESSANDRO, V.; FALONE, M.; GIAMMICHELE, L.; RICCI, R. Eulerian-Lagrangian modeling of cough droplets irradiated by ultraviolet-C light in relation to SARS-CoV-2 transmission. **Physics of Fluids**, v. 33, n. 3, 031905, 2021. DOI: https://doi.org/10.1063/5.0039224.

DBOUK, T.; DRIKAKIS, D. On coughing and airborne droplet transmission to humans. **Physics of Fluids**, v. 32, n. 5, 053310, 2020. DOI: https://doi.org/10.1063/5.0011960.

DHAND, R.; LI, J. Coughs and sneezes: their role in transmission of respiratory viral infections, including SARS-CoV-2. **American Journal of Respiratory and Critical Care Medicine**, v. 202, n. 5, p. 651-659, 2020. DOI: https://doi.org/10.1164/rccm.202004-1263PP.

ELGHANNAY, H. A.; TAFTI, D. K. Revised partial coupling in fluid-particulate systems. **The Journal of Computational Multiphase Flows**, v. 10, n. 4, p. 215-227, 2018. DOI: https://doi.org/10.1177/1757482X18791885.

FENG, Y.; LI, D.; MARCHISIO, D.; VANNI, M.; BUFFO, A. A computational fluid dynamics: population balance equation approach for evaporating cough droplets transport. **International Journal of Multiphase Flow**, v. 165, 104500, 2023. DOI: https://doi.org/10.1016/j.ijmultiphaseflow.2023.104500.

GE, H.; ZHAO, P.; CHOI, S.; DENG, T.; FENG, Y.; CUI, X. Effects of face shield on an emitter during a cough process: a large-eddy simulation study. **Science of The Total Environment**, v. 831, 154856, 2022. DOI: https://doi.org/10.1016/j.scitotenv.2022.154856.

GRALTON, J.; TOVEY, E.; MCLAWS, M.-L.; RAWLINSON, W. D. The role of particle size in aerosolised pathogen transmission: a review. **Journal of Infection**, v. 62, n. 1, p. 1-13, 2011. DOI: https://doi.org/10.1016/j.jinf.2010.11.010.

GUERRA, V. G.; ACHILES, A. E.; BÉTTEGA, R. Influence of droplet size distribution on liquid dispersion in a Venturi scrubber: experimental measurements and CFD simulation. **Industrial & Engineering Chemistry Research**, v. 56, n. 8, p. 2177-2187, 2017. DOI: https://doi.org/10.1021/acs.iecr.6b03761.

GUPTA, J. K.; LIN, C.-H.; CHEN, Q. Flow dynamics and characterization of a cough. **Indoor Air – International Journal of Indoor Environment and Health**, v. 19, n. 6, p. 517-525, 2009. DOI: https://doi.org/10.1111/j.1600-0668.2009.00619.x.

HAN, Z. Y.; WENG, W. G.; HUANG, Q. Y. Characterizations of particle size distribution of the droplets exhaled by sneeze. **Journal of the Royal Society Interface**, v. 10, n. 88, 20130560, 2013. DOI: https://doi.org/10.1098/rsif.2013.0560.

HINDS, W. C.; ZHU, Y. **Aerosol technology**: properties, behavior, and measurement of airborne particles. 3. ed. Hoboken, NJ: Wiley, 2022.

HONKINEN, M.; LAHTI, E.; ÖSTERBACK, R.; RUUSKANEN, O.; WARIS, M. Viruses and bacteria in sputum samples of children with community-acquired pneumonia. **Clinical Microbiology and Infection**, v. 18, n. 3, p. 300-307, 2012. DOI: https://doi.org/10.1111/j.1469-0691.2011.03603.x.

HÖPPE, P. Temperatures of expired air under varying climatic conditions. **International Journal of Biometeorology**, v. 25, p. 127-132, 1981. DOI: https://doi.org/10.1007/BF02184460.

KAMPF, G.; TODT, D.; PFAENDER, S.; STEINMANN, E. Persistence of coronaviruses on inanimate surfaces and their inactivation with biocidal agents. **Journal of Hospital Infection**, v. 104, n. 3, p. 246-251, 2020. DOI: https://doi.org/10.1016/j.jhin.2020.01.022.

KUCHARSKI, A. J.; KLEPAC, P.; CONLAN, A. J.; KISSLER, S. M.; TANG, M. L.; FRY, H.; GOG, J. R.; EDMUNDS, W. H. Effectiveness of isolation, testing, contact tracing, and physical distancing on reducing transmission of SARS-CoV-2 in different settings: a mathematical modelling study. **The Lancet Infectious Diseases**, v. 20, n. 10, p. 1151-1160, 2020. DOI: https://doi.org/10.1016/s1473-3099(20)30457-6.

LANCMANOVÁ, A.; BODNÁR, T. Numerical simulations of human respiratory flows: a review. **Discover Applied Sciences**, v. 7, 242, 2025. DOI: https://doi.org/10.1007/s42452-025-06617-x.

LEE, J.; YOO, D.; RYU, S.; HAM, S.; LEE, K.; YEO, M.; MIN, K.; YOON, C. Quantity, size distribution, and characteristics of cough-generated aerosol produced by patients with an upper respiratory tract infection. **Aerosol and Air Quality Research**, v. 19, n. 4, p. 840-853, 2019. DOI: https://doi.org/10.4209/aaqr.2018.01.0031.

LI, H.; LEONG, F. Y.; XU, G.; GE, Z.; KANG, C. W.; LIM, K. H. Dispersion of evaporating cough droplets in tropical outdoor environment. **Physics of Fluids**, v. 32, n. 11, 113301, 2020. DOI: https://doi.org/10.1063/5.0026360.

LI, X.; SHANG, Y.; YAN, Y.; YANG, L.; TU, J. Modelling of evaporation of cough droplets in inhomogeneous humidity fields using the multi-component Eulerian-Lagrangian approach. **Building and Environment**, v. 128, p. 68-76, 2018. DOI: https://doi.org/10.1016/j.buildenv.2017.11.025.

MAGAR, A. M.; JOSHI, M.; RAJAGOPAL, P. S.; KHAN, A.; RAO, M. M.; SAPRA, B. K. CFD simulation of the airborne transmission of COVID-19 vectors emitted during respiratory mechanisms: revisiting the concept of safe distance. **ACS Omega**, v. 6, n. 26, p. 16876-16889, 2021. DOI: https://doi.org/10.1021/acsomega.1c01489.

MENTER, F. R.; KUNTZ, M.; LANGTRY, R. Ten years of industrial experience with the SST turbulence model. **Turbulence, Heat and Mass Transfer**, v. 4, n. 1, p. 625-632, 2003. Available at: https://www.researchgate.net/profile/Florian-Menter/publication/228742295_Ten_years_of_industrial_experience_with_the_SST_turbulence_model/links/0046353c6330b1c0a4000000/Ten-years-of-industrial-experience-with-the-SST-turbulence-model.pdf. Accessed on: 26 Jan. 2025.

MISHRA, N. P.; DAS, S. S.; YADAV, S.; KHAN, W.; AFZAL, M.; ALARIFI, A.; KENAWY, E.-R.; ANSARI, M. T.; HASNAIN, M. S.; NAYAK, A. K. Global impacts of pre- and post-COVID-19 pandemic: focus on socio-economic consequences. **Sensors International**, v. 1, 100042, 2020. DOI: https://doi.org/10.1016/j.sintl.2020.100042.

MORAWSKA, L. Droplet fate in indoor environments, or can we prevent the spread of infection? **Indoor Air – International Journal of Indoor Environment and Health**, v. 16, p. 335-347, 2006. DOI: https://doi.org/10.1111/j.1600-0668.2006.00432.x.

NICAS, M.; NAZAROFF, W. W.; HUBBARD, A. Toward understanding the risk of secondary airborne infection: emission of respirable pathogens. **Journal**

of Occupational and Environmental Hygiene, v. 2, n. 3, p. 143-154, 2005. DOI: https://doi.org/10.1080/15459620590918466.

NINGTHOUJAM, R. COVID 19 can spread through breathing, talking, study estimates. **Current Medicine Research and Practice**, v. 10, n. 3, p. 132-133, 2020. DOI: https://doi.org/10.1016/j.cmrp.2020.05.003.

NORVIHOHO, L. K.; YIN, J.; ZHOU, Z.-F.; HAN, J.; CHEN, B.; FAN, L.-H.; LICHTFOUSE, E. Mechanisms controlling the transport and evaporation of human exhaled respiratory droplets containing the severe acute respiratory syndrome coronavirus: a review. **Environmental Chemistry Letters**, v. 21, p. 1701-1727, 2023. DOI: https://doi.org/10.1007/s10311-023-01579-1.

OH, W.; OOKA, R.; KIKUMOTO, H.; HAN, M. Numerical modeling of cough airflow: Establishment of spatial-temporal experimental dataset and CFD simulation method. **Building and Environment**, v. 207, Part b, 108531, 2022. DOI: https://doi.org/10.1016/j.buildenv.2021.108531.

PAN, Y.; ZHANG, H.; NIU, Z.; AN, Y.; CHEN, C. Boundary conditions for exhaled airflow from a cough with a surgical or N95 mask. **Indoor Air**, v. 32, n. 8, e13088, 2022. DOI: https://doi.org/10.1111/ina.13088.

PATANKAR, S. V. **Numerical heat transfer and fluid flow**. Boca Raton: CRC Press, 1980. DOI: https://doi.org/10.1201/9781482234213.

PERELLA, P.; TABARRA, M.; HATAYSAL, E.; POURNASR, A.; RENFREW, I. Minimising exposure to droplet and aerosolised pathogens: a computational fluid dynamics study. **British Journal of Anaesthesia**, v. 126, n. 2, p. 544-549, 2021. DOI: https://doi.org/10.1016/j.bja.2020.09.047.

POKHAREL, A.; AKKERMAN, V.; CELIK, I. B.; AXELBAUM, R. L.; ISLAS, A.; YANG, Z. Impact of particle loading and phase coupling on gas–solid flow dynamics: a case study of a two-phase, gas-solid flow in an annular pipe. **Physics of Fluids**, v. 33, n. 7, 073308, 2021. DOI: https://doi.org/10.1063/5.0054906.

REDROW, J.; MAO, S.; CELIK, I.; POSADA, J. A.; FENG, Z.-G. Modeling the evaporation and dispersion of airborne sputum droplets expelled from a human cough. **Building and Environment**, v. 46, n. 10, p. 2042-2051, 2011. DOI: https://doi.org/10.1016/j.buildenv.2011.04.011.

ROACHE, P. J. **Verification and validation in computational science and engineering**. Albuquerque: Hermosa, 1998.

SANTANA, H. S.; SILVA, A. G. P.; LOPES, M. G. M.; RODRIGUES, A. C.; TARANTO, O. P.; SILVA JUNIOR, J. L. Computational methodology for the development of microdevices and microreactors with ANSYS CFX. **MethodsX**, v. 7, 100765, 2020. DOI: https://doi.org/10.1016/j.mex.2019.12.006.

SCHARFMAN, B. E.; TECHET, A. H.; BUSH, J. W. M.; BOUROUIBA, L. Visualization of sneeze ejecta: steps of fluid fragmentation leading to respiratory droplets. **Experiments in Fluids**, v. 57, 24, 2016. DOI: https://doi.org/10.1007/s00348-015-2078-4.

SCHILLER, L.; NAUMANN, A. A drag coefficient correlation. **Zeitschrift des Vereins Deutscher Ingenieure**, v. 77, p. 318-320, 1935.

SHYY, W.; THAKUR, S.; WRIGHT, J. Second-order upwind and central difference schemes for recirculating flow computation. **AIAA Journal**, v. 30, n. 4, p. 923-932, 1992. DOI: https://doi.org/10.2514/3.11010.

SIRIGNANO, W. A. **Fluid dynamics and transport of droplets and sprays**. Cambridge, UK: Cambridge University Press, 2009. DOI: https://doi.org/10.1017/CBO9780511529566.

SONNTAG, D.; FOKEN, T.; VÖMEL, H.; HELLMUTH, O. Humidity sensors. *In*: FOKEN, T. (ed.). **Springer handbook of atmospheric measurements**. Cham: Springer International Publishing, 2021. p. 209-241. DOI: https://doi.org/10.1007/978-3-030-52171-4_8.

TAKII, A.; YAMAKAWA, M.; KITAGAWA, A.; WATAMURA, T.; CHUNG, Y. M.; KIM, M. Numerical model for cough-generated droplet dispersion on moving escalator with multiple passengers. **Indoor Air**, v. 32, n. 11, e13131, 2022. DOI: https://doi.org/10.1111/ina.13131.

THAKUR, N.; MURTHY, H. Simulation study of droplet formation in inkjet printing using ANSYS FLUENT. **Journal of Physics: Conference Series**, v. 2161, 012026, 2022. DOI: https://doi.org/10.1088/1742-6596/2161/1/012026.

TOM, J.; CARBONE, M.; BRAGG, A. D. How does two-way coupling modify particle settling and the role of multiscale preferential sweeping? **Journal of Fluid Mechanics**, v. 947, A7, 2022. DOI: https://doi.org/10.1017/jfm.2022.615.

TRIVEDI, S.; GKANTONAS, S.; MESQUITA, L. C. C.; IAVARONE, S.; OLIVEIRA, P. M.; MASTORAKOS, E. Estimates of the stochasticity of droplet dispersion by a cough. **Physics of Fluids**, v. 33, n. 11, 115130, 2021. DOI: https://doi.org/10.1063/5.0070528.

VAN DER REIJDEN, W. A.; VEERMAN, E. C. I.; AMERONGEN, A. V. N. Shear rate dependent viscoelastic behavior of human glandular salivas. **Biorheology**, v. 30, n. 2, p. 141-152, 1993. DOI: https://doi.org/10.3233/BIR-1993-30205.

VEJERANO, E. P.; MARR, L. C. Physico-chemical characteristics of evaporating respiratory fluid droplets. **Journal of The Royal Society Interface**, v. 15, n. 139, 20170939, 2018. DOI: https://doi.org/10.1098/rsif.2017.0939.

VERSTEEG, H. K.; MALALASEKERA, W. **An introduction to computational fluid dynamics**: The Finite Volume Method. 2nd ed. Harlow: Pearson Education, 2007.

WAI, K.-M.; YUAN, C.; LAI, A.; YU, P. K. N. Relationship between pedestrian-level outdoor thermal comfort and building morphology in a high-density city. **Science of the Total Environment**, v. 708, 134516, 2020. DOI: https://doi.org/10.1016/j.scitotenv.2019.134516.

WANG, F.; ZENG, Y.; YAN, H. CFD-DEM study of impacts of the porous distributor medium on fluidization characteristics of a 2D-fluidized bed. **Particuology**, v. 87, p. 54-73, 2024. DOI: https://doi.org/10.1016/j.partic.2023.07.017.

WEBER, T. P.; STILIANAKIS, N. I. Inactivation of influenza A viruses in the environment and modes of transmission: a critical review. **Journal of Infection**, v. 57, n. 5, p. 361-373, 2008. DOI: https://doi.org/10.1016/j.jinf.2008.08.013.

WEI, J.; LI, Y. Enhanced spread of expiratory droplets by turbulence in a cough jet. **Building and Environment**, v. 93, Part 2, p. 86-96, 2015. DOI: https://doi.org/10.1016/j.buildenv.2015.06.018.

WEXLER, A; BROMBACHER, W. G. **Methods of Measuring Humidity and Testing Hygrometers**. Washington, D.C.: National Bureau of Standards, 1951. (NBS Circular, 512). Available at: https://www.govinfo.gov/content/pkg/GOVPUB-C13-b587954bfd21b3fddc15dcdfd4256f25/pdf/GOVPUB-C13-b587954bfd21b3fddc15dcdfd4256f25.pdf. Accessed on: 25 Feb. 2026.

WHO – WORLD HEALTH ORGANIZATION. COVID-19 Cases, World. **WHO COVID-19 dashboard**. 2025. Available at: https://data.who.int/dashboards/covid19/cases?n=o. Accessed on: 2 June 2025.

WHO – WORLD HEALTH ORGANIZATION. Tuberculosis control and research strategies for the 1990s: memorandum from a WHO meeting. **Bulletin of the World Health Organization (WHO)**, v. 70, n. 1, p. 17-21, 1992. Available at: https://europepmc.org/article/pmc/2393335. Accessed on: 2 June 2025.

WÖLFEL, R.; CORMAN, V. M.; GUGGEMOS, W.; SEILMAIER, M.; ZANGE, S.; MÜLLER, M. A.; NIEMEYER, D.; JONES, T. C.; VOLLMAR, P.; ROTHE, C.; HOELSCHER, M.; BLEICKER, T.; BRÜNINK, S.; SCHNEIDER, J.; EHMANN, R.; ZWIRGLMAIER, K.; DROSTEN, C.; WENDTNER, C. Virological assessment of hospitalized patients with COVID-2019. **Nature**, v. 581, p. 465-469, 2020. DOI: https://doi.org/10.1038/s41586-020-2196-x.

WU, J.; HE, F.; XIE, Z.; FU, M.; LI, Y.; WANG, J.; PAN, Y.; WENG, W. Review on respiratory infectious disease transmission mechanism: effects of human movement and facemask use. **Emergency Management Science and Technology**, v. 4, e004, 2024. DOI: https://doi.org/10.48130/emst-0024-0006.

YAN, Y.; LI, X.; TU, J. Thermal effect of human body on cough droplets evaporation and dispersion in an enclosed space. **Building and Environment**, v. 148, p. 96-106, 2019. DOI: https://doi.org/10.1016/j.buildenv.2018.10.039.

YANG, S.; LEE, G. W. M.; CHEN, C.-M.; WU, C.-C.; YU, K.-P. The size and concentration of droplets generated by coughing in human subjects. **Journal of Aerosol Medicine and Pulmonary Drug Delivery**, v. 20, n. 4, p. 484-494, 2007. DOI: https://doi.org/10.1089/jam.2007.0610.

ZAHARI, N. M.; ZAWAWI, M. H.; SIDEK, L. M.; MOHAMAD, D.; ITAM, Z.; RAMLI, M. Z.; SYAMSIR, A.; ABAS, A.; RASHID, M. Introduction of discrete phase model (DPM) in fluid flow: a review. **AIP Conference Proceedings**, v. 2030, n. 1, 020234, 2018. DOI: https://doi.org/10.1063/1.5066875.

ZHAO, Y.; CHENG, Y.; WU, C.; DING, Y.; JIN, Y. Eulerian-Lagrangian simulation of distinct clustering phenomena and RTDs in riser and downer. **Particuology**, v. 8, n. 1, p. 44-50, 2010. DOI: https://doi.org/10.1016/j.partic.2009.11.002.

ZODO, G.; KONKA, H.; STEVANOVIC, S.; SCHLUTER, J. Simulation of the transition of respiratory droplets to aerosol states: Implications for pathogen spread. **Physics of Fluids**, v. 37, n. 1, 015188, 2025. DOI: https://doi.org/10.1063/5.0246654.